JOURNAL OF GEOPHYSICAL RESEARCH, VOL. 97, NO. B4, PAGES 4843–4864, APRIL 10, 1992

Seismicity and Geometry of a 110-km-Long Blind Thrust Fault 1. The 1985 Kettleman Hills, California, Earthquake

GÖRAN EKSTRÖM

Department of Earth and Planetary Sciences, Harvard University, Cambridge, Massachusetts

ROSS S. STEIN, J. P. EATON, AND D. EBERHART-PHILLIPS

U.S. Geological Survey, Menlo Park, California

The August 4, 1985, Kettleman Hills earthquake was the third in a sequence of moderate shocks to occur beneath the northern half of a 110-km-long fold chain bounding the eastern California Coast Ranges. The 1982 M_W=5.4 New Idria, 1983 M_W=6.5 Coalinga, and 1985 M_W=6.1 Kettleman Hills events define a southward progression of seismic activity beneath the fold. We use teleseismic waveforms, geodetic modeling, hypocenters relocated in a three-dimensional velocity model, and subsurface structural data to investigate the Kettleman Hills earthquake. The main shock results from motion on a shallowly dipping thrust fault buried at ~10 km depth. Aftershocks and coseismic fault slip extend 20 km along the fold axis, nearly the full extent of the Kettleman Hills North Dome anticline. Aftershocks occur primarily several kilometers in front of the fault tip and in the core of the anticline. The main shock and several foreshocks occurred at a 2-km right step in the Quaternary fold axis, which also corresponds to the southern end of the 1983 Coalinga and northern end of the 1985 Kettleman Hills aftershock zones. From this we infer that the step in the fold is caused by an offset or tear in the underlying fault. The scalar seismic moment is 1.6×10^{18} N m, consistent with the geodetic deformation, and the duration of rupture is 16 s, 3–4 times greater than for the average earthquake with this scalar moment. The slow rate of moment release provides an explanation for the low level of ground shaking and low local magnitude reported for the event. The peak of the geodetic uplift is located 5 km perpendicular to the Quaternary fold axis. We argue that the fault is propagating northeast into the undeformed San Joaquin Valley sediments and that the overlying fold is growing at about 0.5 mm/yr.

INTRODUCTION

The August 4, 1985, M_W=6.1 Kettleman Hills earthquake occurred beneath the Kettleman Hills North Dome anticline, a Plio-Quaternary fold on the western margin of the San Joaquin basin [*Woodring et al.*, 1940]. Previous studies have shown that the earthquake had a thrust focal mechanism [*Ekström*, 1986; J. P. Eaton, unpublished manuscript, 1985], similar in orientation to the May 2, 1983, M_W=6.5 Coalinga earthquake that was located 15 km northwest of the Kettleman Hills earthquake beneath the Coalinga anticline (Figure 1). The Coalinga earthquake [*Stein and King*, 1984], as well as several other events (for example, the 1964 Niigata, Japan, earthquake [*Kawasumi*, 1973], the 1985 Nahanni, Canada, earthquakes [*Wetmiller et al.*, 1988], and the 1987 Whittier Narrows, California, earthquake [*Hauksson and Jones*, 1989; *Lin and Stein*, 1989]), are all examples of buried or "blind" faults which have caused growth of overlying folds. We show in this paper that the Kettleman Hills earthquake also belongs in this category of events. While the association between earthquakes and fold growth [e.g., *Stein and Yeats*, 1989] as well as arguments for [*McGarr*, 1991] and against [*Segall*, 1985] the triggering of earthquakes by extraction of oil from the folds have been pursued in several recent studies, the mechanisms of seismic deformation remain poorly understood. Simple tasks, such as choosing the fault plane from the two nodal planes, are much more difficult for earthquakes on blind faults than for those on surface-cutting faults. Nonplanar distributions of aftershocks contribute to this ambiguity. Typically, the earthquake hypocenter, fault plane locations, and subsurface structure are poorly known, making the correlation between geological and seismic elements tentative. In contrast, the Kettleman Hills earthquake occurred in a region which has been extensively studied, both for oil exploration and to understand the Coalinga earthquake to the north, and the deeper structure is relatively well known.

In this paper we use seismicity, seismic waveforms, geodetic data, and ground shaking intensity data to constrain the faulting parameters and rupture process of the Kettleman Hills earthquake. We combine our analysis with a seismic reflection profile in the source area. We address the question of where seismic activity and coseismic fault slip occurred beneath the fold and how this relates to the surface structures. Reverse faulting on steeply dipping planes [*Stein and King*, 1984], blind thrust faulting on shallow-dipping planes [*Wentworth and Zoback*, 1989, 1990], and fault-bend folding [*Namson and Davis*, 1988] have all been proposed as the underlying mechanism of earthquake-related growth of folds at different locations. By adding the unusually complete set of observations for the Kettleman Hills earthquake to this debate, we can attempt to resolve this question.

The Kettleman Hills earthquake and the Coalinga shock appear to be part of a sequence of fold-related earthquakes along the 110-km-long chain of anticlines which runs parallel to the western edge of the San Joaquin Valley (Figure 1). The sequence started with the October 25, 1982, M_W=5.4 New Idria earthquake, which occurred beneath the New Idria anticline, a northward en echelon continuation of the Coalinga anticline. The May 2, 1983, M_W=6.5 Coalinga,

Paper number 91JB02925.
0148-0227/92/91JB-02925$05.00

and the August 4, 1985, M_W=6.1 Kettleman Hills earthquakes form the southward continuation of this sequence. In a companion study [*Stein and Ekström*, this issue] we discuss the Kettleman Hills earthquake in its broader context and explore the possibility that an active fault underlies this 110-km-long chain of growing folds.

The Kettleman Sequence

The Kettleman Hills earthquake sequence started on August 3, 1985, with a small number of foreshocks in the immediate neighborhood of the main shock hypocenter. An earthquake with magnitude M=4.1 occurred 22 hours before the main shock, and the largest foreshock (M=4.6) occurred 30 min before the main shock. The six foreshocks locate within 2 km of the main shock. The main shock (August 4, 1985, 1201:55.94, 36°7.11′N, 120°8.97′W, h=10.1 km) had teleseismic magnitudes m_b=5.4 and M_S=5.8. Local magnitude estimates range from M_L=5.4 to M_L=5.9. To supplement the stations of the Northern California Seismic Network (Calnet), a set of portable instruments was installed by the U.S. Geological Survey (USGS) on August 5. These were deployed primarily in the San Joaquin Valley (Figure 1) and operated for about 2 weeks. In the 4-week period following the main shock, approximately 400 aftershocks occurred which could be located. We have relocated the earthquake sequence in a three-dimensional velocity model and have redetermined focal mechanisms for 30 of the best recorded events using P wave first motions.

Earthquake Locations

For 42 larger well-recorded events, seismograms from the network and temporary stations were read by hand. In addition to P and S arrival times, maximum amplitude and corresponding periods were read and used to determine a local amplitude based magnitude (M) [see *Eaton et al.*, 1970]. For the remaining events the network phases were analyzed manually, while phases recorded on the temporary stations were timed by computer using the Allen/Ellis real time processor [*Allen*, 1982]. Magnitudes for these events were calculated from the coda durations. The sequence was originally located in a one-dimensional crustal velocity model developed for the Coalinga area [*Hill et al.*, 1990; J. P. Eaton, unpublished manuscript, 1985]. We relocate the events in the three-dimensional velocity structure model determined by *Eberhart-Phillips* [1989*b*] in a study of the Coalinga earthquake sequence. This model was obtained using Coalinga and Kettleman Hills aftershocks as well as a line of refraction shots that sample the spatial velocity field across the Coalinga anticline. The spacing of the velocity model grid is smallest at Coalinga and greater beneath Kettleman Hills North Dome and farther south. The lateral heterogeneity of the three-dimensional velocity model diminishes to the south, and the model approaches a multilayered one-dimensional model. We expect that the accuracy of our locations decreases with the distance from the Coalinga aftershock zone, where the velocity structure is best constrained.

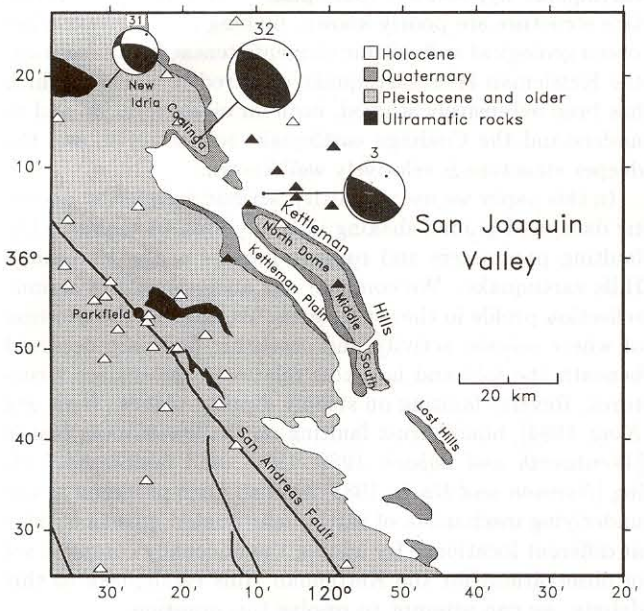

Fig. 1. Map showing the surface geology of the study area. The permanent stations of the Northern California Seismic Network used in locating the Kettleman Hills earthquake sequence are shown as open triangles; solid triangles show the locations of the temporarily deployed instruments. Equal-area, lower hemisphere projections of the focal sphere for the 1982 New Idria, 1983 Coalinga, and 1985 Kettleman Hills earthquakes are also shown, where the compressional quadrants are shaded. The focal mechanism for the Kettleman Hills earthquake was obtained from waveform inversion. The event numbers refer to Table 1.

The sequence was located using the same computer code that was previously employed to determine the three-dimensional structure and to locate the Coalinga earthquake sequence [*Eberhart-Phillips*, 1989*a*, *b*; *Thurber*, 1983]. Stations with an epicentral distance of 80 km or less were used in the hypocenter determination, and a reading error of 0.1 s in the phase arrival times was used in estimating the uncertainty ellipsoids for the locations. Only P phases were used.

We performed several experiments in which we compared the locations obtained from standard one-dimensional location algorithms (HYPO71, HYPOINVERSE) with our new locations. Relative event locations in general did not change by more than 1 km, but the three-dimensional model produced a systematic 2-km shift of the hypocenters toward the south. A few events moved as much as 4 km. In map view and cross section the three-dimensional event locations cluster more tightly, although the overall spatial pattern is unchanged. In a different experiment we used the three-dimensional velocity model and derived a set of station corrections for the Kettleman Hills sequence from the best recorded events. These station corrections were then used in a relocation of the whole sequence. The effect of introducing station corrections was primarily to produce a systematic shift of the locations by less than 1 km in a southwestern direction.

We concluded that the effect of relocation is modest for most events, about 2 km. The locations in the three-dimensional velocity model are probably better than the one-dimensional alternative, since the three-dimensional model was derived using both fixed sources and earthquakes recorded throughout the region of interest. We decided not to use station corrections, since the benefit seemed small, and their inclusion would make it more difficult to discuss the location of some northerly Kettleman Hills events relative to the previously located Coalinga events.

Earthquake locations in map view. Figure 2*a* shows the well-located events of the sequence in map view. Only events with horizontal and vertical errors less than 1.5 km are plotted. Before relocation the main shock had located adjacent

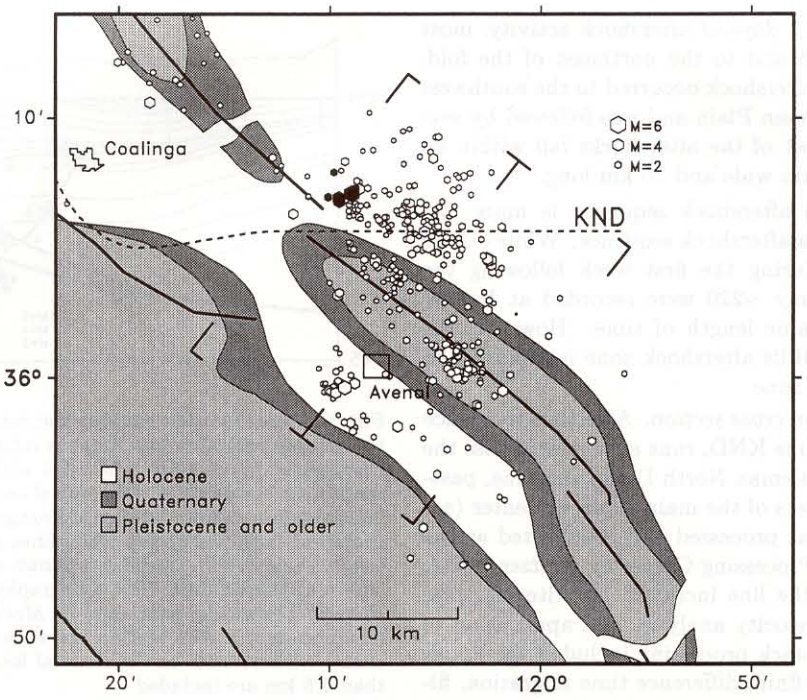

Fig. 2*a*. Map showing the Kettleman Hills aftershock sequence. The foreshock and main shock symbols are solid. The dashed line shows the location of the KND reflection line analyzed by *Meltzer* [1989]. The brackets indicate the locations of a northwestern and a southeastern section of seismicity which are viewed in cross section in Figures 3*b* and 3*c*.

to the Coalinga fold; it is now located 5–6 km northeast of the fold axis at the northern end of the North Kettleman Hills anticline, where a 2-km step occurs between the southern end of the Coalinga anticline and the northern end of the Kettleman Hills anticline. Six foreshocks were recorded, four during the 30 min preceding the main shock. All locate within approximately 2 km of the main shock.

Within hours of the main shock, aftershocks extended approximately 20 km along the strike of the fold axis. A few isolated events occurred up to 30 km south of the main

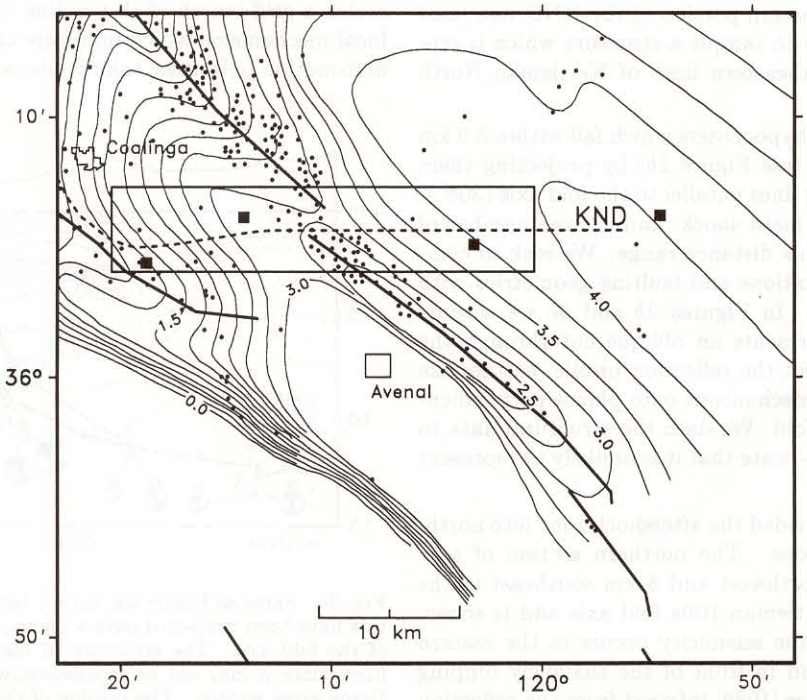

Fig. 2*b*. Map showing the structure contour map of the depth (in kilometers) to the top of the Kreyenhagen Formation [from *Zigler et al.*, 1986]. Dots show the locations of wells which reach the top of the Kreyenhagen Formation. The location of the KND seismic reflection line is shown, as well as the locations of four wells (solid squares) that were used by *Meltzer* [1989] to determine the time-to-depth conversion for the reflection profile. The box shows the borders of the seismicity viewed in cross section in Figure 3*a*.

shock. During the first 3 days of aftershock activity, most events occurred beneath and to the northeast of the fold. On August 7 a M=4.6 aftershock occurred to the southwest of the fold in the Kettleman Plain and was followed by several smaller shocks. Most of the aftershocks fall within an area approximately 10 km wide and 20 km long.

The Kettleman Hills aftershock sequence is more dispersed than the Coalinga aftershock sequence. While ~2600 events were recorded during the first week following the Coalinga earthquake, only ~220 were recorded at Kettleman Hills during the same length of time. However, the area of the Kettleman Hills aftershock zone is almost 50% the size of the Coalinga zone.

Earthquake locations in cross section. A vertical incidence seismic profile, Conoco line KND, runs east–west across the northern end of the Kettleman North Dome anticline, passing within a few kilometers of the main shock epicenter (see Figure 2*a*). This line was processed and interpreted at the Rice Geophysical Data Processing Center by *Meltzer* [1989]. Prestack processing of the line included f-k filtering, predictive deconvolution, velocity analysis, and application of static corrections. Poststack processing included the application of datum statics, finite difference time migration, filter, and display. The velocity structure used in the time-to-depth conversion was further constrained by sonic logs of several deep wells shown in Figure 2*b*, as well as by waveform modeling of a wide-angle reflection-refraction profile across the Coalinga anticline.

The KND line crosses the northwestern plunge of the Kettleman Hills structure, and the western half of the profile is probably not representative of the Kettleman North Dome structure. Surface geology and well data [*Zigler et al.*, 1986] suggest that the subsurface structure of Kettleman Hills anticline is continuous and varies little along the strike of the fold (Figure 2*b*). The eastern portion of the KND line (east of the fold axis) is likely to sample a structure which is representative for the northeastern limb of Kettleman North Dome.

In Figure 3*a* we show hypocenters which fall within 3.0 km of the reflection profile (see Figure 2*b*) by projecting them onto the structure along lines parallel to the fold axis (308°). Several foreshocks, the main shock, and a large number of aftershocks lie within this distance range. We seek to compare the earthquake locations and faulting geometries with the inferred structures. In Figures 3*b* and 3*c* we assume that the KND line represents an oblique cut through the structure, and we project the reflection profile, earthquake hypocenters, and focal mechanisms onto planes perpendicular to the strike of the fold. We dash the structural data to the west of the fold to indicate that it is unlikely to represent the true structure.

For clarity we have divided the aftershock zone into northern and southern sections. The northern section of seismicity extends 2 km northwest and 8 km southeast of the northern tip of the Kettleman Hills fold axis and is shown in Figure 3*b*. Most of the seismicity occurs in the eastern limb of the anticline and in front of the shallowly dipping thrust faults that *Meltzer* [1989] inferred from the reflection profile. Some events are as much as 10 km to the northeast of the fold axis. A group of aftershocks is centered in the core of the anticline, where the shallowest events occur. The deepest events occur 7–9 km southwest of the anticline axis.

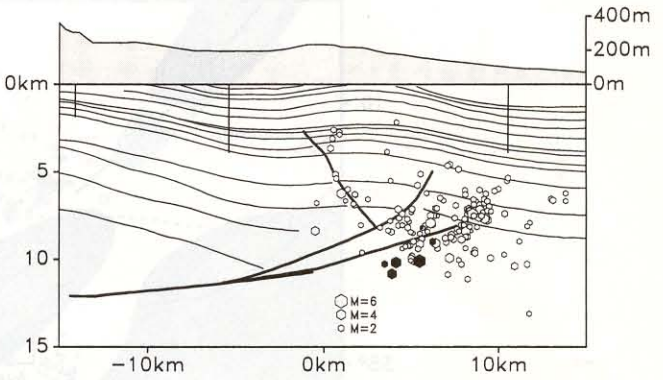

Fig. 3*a*. Cross section showing the subsurface structure beneath the seismic reflection line KND as interpreted by *Meltzer* [1989]. Earthquake hypocenters which fall within 3.0 km horizontal distance from the vertical profile are shown. The foreshocks and the main shock are shown with solid hexagons. The hypocenters were projected onto the profile along lines parallel with the strike of the fold axis (308°). Bedding is shown as thin lines, and faults are shown as thicker lines. The topography is shown above the cross section. Three deep wells used by *Meltzer* [1989] to constrain the interpretation of the section are shown as vertical lines. Only events with vertical and horizontal location uncertainties of less than 1.5 km are included.

The southern section (see Figure 2*a*) of seismicity extends from 8 to 18 km southeast along the anticline and is shown in Figure 3*c*. The activity here is deeper and there are more events directly beneath the anticline.

Focal Mechanisms

We determined first-motion focal mechanisms for a subset of well-recorded events using the computer program FPFIT [*Reasenberg and Oppenheimer*, 1985]. This algorithm makes a grid search of all possible fault angles and finds the focal mechanisms which minimize the number of discrepant first-motion polarities, taking into account the quality of the

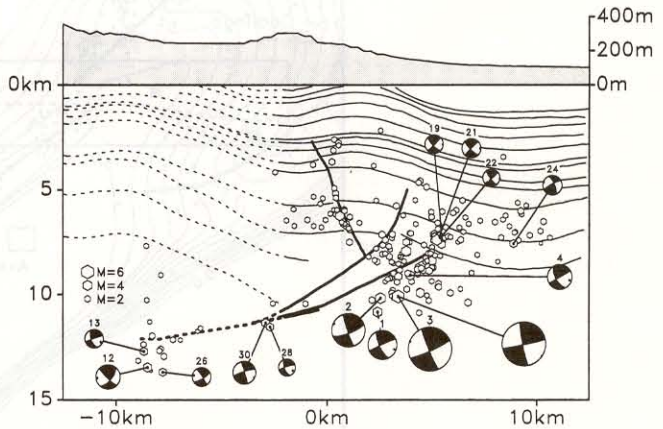

Fig. 3*b*. Same as Figure 3*a*, except both structure and hypocenters have been projected onto a plane perpendicular to the strike of the fold axis. The structure to the west is shown as dashed lines, since it may not be representative of the Kettleman North Dome cross section. The outline of the section of included seismicity is shown in map view by the northwestern brackets in Figure 2*a*. First motion focal mechanisms are shown in back-hemisphere projection and the event numbers refer to Table 1. The unlabeled focal mechanism is the preferred solution for the main shock (event 3), obtained by waveform inversion.

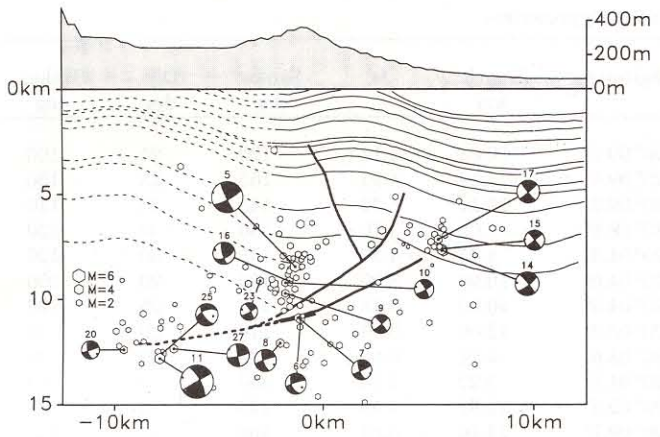

Fig. 3c. As Figure 3b, but for the southeastern section of seismicity (Figure 2a).

reading and the proximity of the departing ray to the nodal planes. Takeoff directions for the rays at the source were calculated in the heterogeneous velocity structure. We initially studied 42 events but eliminated 12 of these with ambiguous solutions, or those we thought otherwise unreliable. The 30 remaining solutions are shown in map view in Figure 4 and the source parameters are listed in Table 1. All the events show thrust or reverse mechanisms on faults striking approximately northwest–southeast. Mechanisms with one nodal plane dipping at a shallow angle to the southwest dominate, but higher angle dips are also present. Viewing the focal mechanisms in cross section (Figures 3b and 3c), the shallower events tend to have steeper dip angles, in some cases correlating with the steepening of imaged faults [*Meltzer*, 1989] splaying toward the surface.

The focal mechanism for the main shock has one nodal plane with a dip of 25°, more steeply dipping than the mechanism determined by J. P. Eaton (as cited by *Hill et al.* [1990]), who reported a dip of 12° for an otherwise similarly oriented plane. The difference is primarily caused by the different velocity structures employed, since we used the same data set as Eaton. We note that small changes in P wave velocity in the source region can cause large changes in the dip angle for rays departing almost horizontally. For dip-slip mechanisms these rays often constrain the dip of the shallowly dipping nodal plane, which consequently has a large uncertainty associated with it.

Teleseismic Analysis of the Main Shock

The Kettleman Hills main shock was well recorded on globally distributed digital seismic stations. We have analyzed the long-period body waves (periods greater than 45 s) and surface waves (period greater than 135 s) using the centroid moment tensor (CMT) algorithm of *Dziewonski et al.* [1981] and *Dziewonski and Woodhouse* [1983]. This analysis provides estimates of the focal mechanism, in terms of a moment tensor, and a source centroid, which is the point location in space and time that provides the best correlation between synthetic and observed seismograms. The moment tensor represents a nearly pure double-couple source (Table 1), with one plane dipping very shallowly (12°) toward

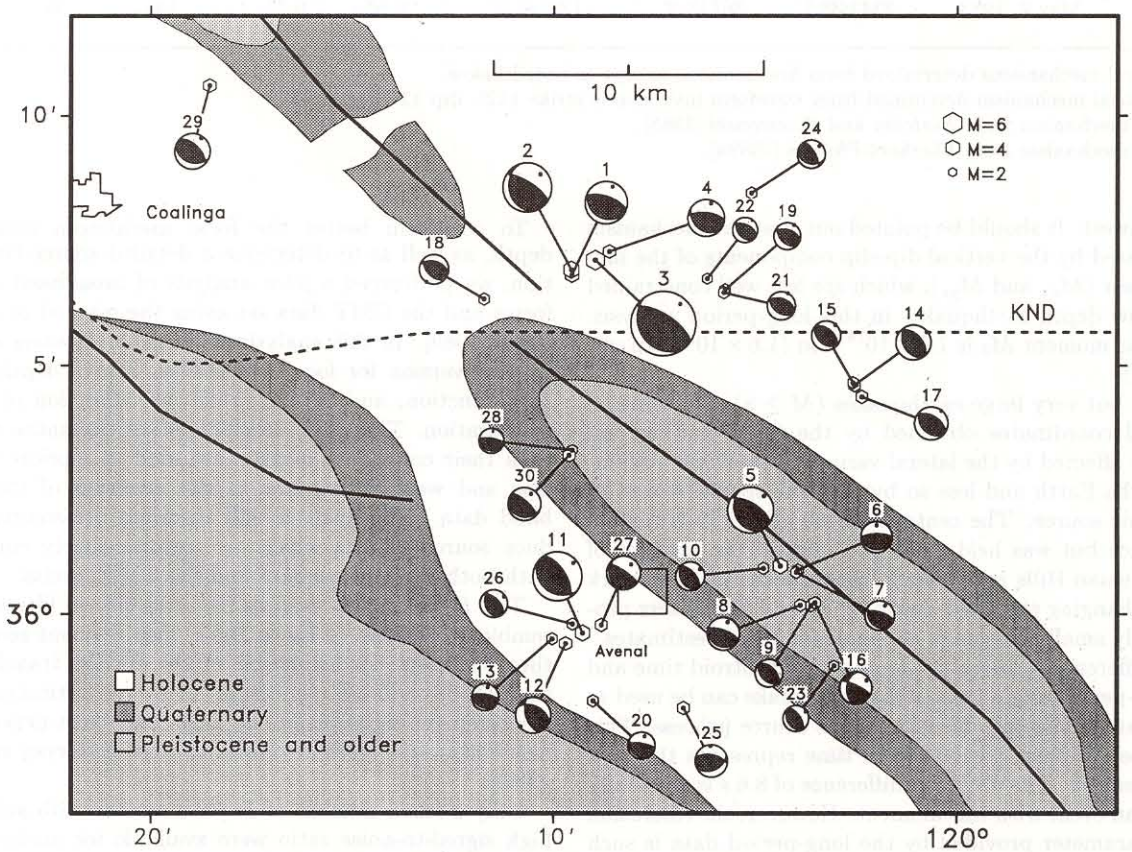

Fig. 4. Map view showing the locations and focal mechanisms of 30 events with well-constrained solutions. The numbers refer to Table 1. The location of the KND reflection line is also shown.

TABLE 1. Relocated Hypocenters

No.	Date	Time, UT	Latitude	Longitude	Depth, km	M	Strike, deg	Dip, deg	Rake, deg
1	Aug. 3, 1985	1357:10.5	36°06.8′	−120°09.6′	10.83	4.11	120	25	100
2	Aug. 4, 1985	1129:14.9	36°06.9′	−120°09.6′	10.18	4.61	165	25	130
3[a]	Aug. 4, 1985	1201:55.5	36°07.1′	−120°09.0′	10.10	5.72	145	25	110
4	Aug. 4, 1985	1309:18.8	36°07.3′	−120°08.6′	9.09	3.70	130	30	120
5	Aug. 4, 1985	1515:39.0	36°01.0′	−120°04.4′	8.45	4.37	155	30	120
6	Aug. 4, 1985	1734:41.4	36°00.9′	−120°04.0′	10.98	3.30	100	20	100
7	Aug. 4, 1985	2215: 0.2	36°00.8′	−120°04.0′	10.89	3.18	140	25	120
8	Aug. 4, 1985	2345:51.1	36°00.2′	−120°03.9′	12.09	3.39	110	20	90
9	Aug. 5, 1985	0303:12.9	36°00.2′	−120°03.6′	9.72	3.06	135	40	90
10	Aug. 6, 1985	1811:13.5	36°00.9′	−120°04.8′	9.22	3.14	150	30	100
11	Aug. 7, 1985	0016: 3.3	35°59.6′	−120°09.3′	12.82	4.59	125	30	70
12	Aug. 7, 1985	0028:12.4	35°59.4′	−120°09.7′	13.46	3.61	160	55	120
13	Aug. 7, 1985	0312:33.3	35°59.5′	−120°10.0′	12.70	3.01	120	20	110
14	Aug. 9, 1985	0847: 9.5	36°04.6′	−120°02.5′	7.69	3.57	150	40	100
15	Aug. 9, 1985	0900:35.9	36°04.7′	−120°02.6′	7.61	3.17	130	40	90
16	Aug. 9, 1985	0955: 7.2	36°00.2′	−120°03.5′	9.15	3.39	295	75	50
17	Aug. 9, 1985	1115:33.1	36°04.4′	−120°02.3′	7.16	3.46	135	40	100
18	Aug. 11, 1985	0630:24.7	36°06.3′	−120°11.7′	8.38	3.18	135	50	110
19	Aug. 12, 1985	2209: 9.9	36°06.5′	−120°05.8′	7.42	3.01	135	45	110
20	Aug. 12, 1985	2349:59.4	35°58.3′	−120°09.0′	12.40	3.01	280	75	80
21	Aug. 14, 1985	2329:55.3	36°06.5′	−120°05.8′	7.22	3.09	125	45	100
22	Aug. 16, 1985	2308:32.9	36°06.7′	−120°06.2′	7.30	2.88	140	40	110
23	Aug. 22, 1985	0009:22.0	35°59.0′	−120°03.0′	9.12	2.91	145	30	90
24	Aug. 27, 1985	1830:51.8	36°08.4′	−120°05.1′	7.57	3.11	105	30	50
25	Aug. 27, 1985	1902: 7.4	35°58.1′	−120°06.8′	12.57	3.42	65	40	60
26	Sept. 6, 1985	0432:25.1	35°59.8′	−120°09.5′	13.69	3.04	160	35	110
27	Sept. 8, 1985	1217:17.1	35°59.8′	−120°08.8′	12.35	3.47	165	15	130
28	Sept. 12, 1985	0029:15.5	36°03.3′	−120°09.5′	11.54	2.85	100	20	90
29	Sept. 14, 1985	0302:44.6	36°10.6′	−120°18.5′	10.92	3.62	110	35	70
30	Sept. 15, 1985	0909:46.8	36°03.2′	−120°09.6′	11.35	3.46	100	20	60
31[b]	Oct. 25, 1982	2226: 3.8	36°19.0′	−120°30.4′	13.95	4.60	154	41	137
32[c]	May 2, 1983	2342:38.1	36°13.3′	−120°17.5′	9.65	6.70	145	30	100

All focal mechanisms determined from first motions except as noted below.
[a]The focal mechanism detemined from waveform inversion is strike 142°, dip 12°, rake 109°.
[b]Focal mechanism from *Ekström and Dziewonski* [1985].
[c]Focal mechanism from *Eberhart-Phillips* [1989*a*].

the southwest. It should be pointed out that the mechanism is dominated by the vertical dip-slip components of the moment tensor (M_{xz} and M_{yz}), which are less well constrained for shallow depth earthquakes in this long-period analysis. The scalar moment M_0 is 1.6×10^{18} N m (1.6×10^{25} dyn cm, M_W=6.1).

For all but very large earthquakes ($M \geq 8$), the centroid epicentral coordinates obtained by the CMT method are primarily affected by the lateral variations in elastic parameters in the Earth and less so by the true spatial extent of the seismic source. The centroid depth generally has more significance but was held fixed at 11 km in the analysis of the Kettleman Hills main shock based on the local network depth. Changing the fixed depth by several kilometers produced only small changes in the moment tensor estimates.

The difference between the long-period centroid time and the short-period origin time of the earthquake can be used as an estimate of the half duration of the source process. This is because the short-period origin time represents the rupture nucleation. The obtained difference of 8.6 s is unusually large for an event with this moment. However, the resolution of this parameter provided by the long-period data is such that the large value could be attributed to the combined effect of station coverage and unmodeled heterogeneous velocity structure of the Earth.

To constrain better the focal mechanism and source depth, as well as to determine a detailed source time function, we performed a joint analysis of broadband P waveforms and the CMT data set using the method of *Ekström* [1987, 1989]. In this analysis, teleseismic P waves are used in an inversion for focal mechanism, source depth, source time function, and, as an option, the direction of rupture propagation. The CMT moment tensor estimates, together with their covariance matrix, are used as a priori information and weak constraints in the inversion of the broadband data. The analysis will therefore preferentially produce source models which are simultaneously compatible with both the P wave data and the CMT results.

The P waveforms used in the analysis are filtered to resemble broadband (1 Hz to 100 s) displacement records, either by direct deconvolution of the station transfer function (for broadband recordings) or by reconstitution of the displacement signal from the long- and short-period channels following a method similar to that of *Harvey and Choy* [1982].

Only a small number of P wave records with sufficiently high signal-to-noise ratio were available for analysis. The low signal levels at higher frequencies are unusual for an earthquake of this size but are consistent with a long source duration since, for a given scalar moment, the displacement

amplitude of a single P wave pulse is inversely proportional to the source duration. Broadband records were successfully deconvolved for seven stations (Figure 5). Due to the higher noise level and difficulties identifying the onset of the signal at GRFO, KONO and TOL, these stations were not used in the waveform inversion. The response at the source was calculated by a layer matrix method for a flat-layered crustal model developed in the analysis of the Coalinga aftershocks [*Eaton*, 1990]. This model includes a 2-km-thick sediment layer and three layers of increasing crustal velocities with depth. The details of the crustal model are not critical in modeling the teleseismic waveforms, and similar results were obtained for a single-layer crustal model with average elastic properties. Comparisons of observed and synthetic seismograms, as well as the focal mechanism and source time function, are shown in Figure 5. The fits are good at HRV, SCP, and COL, which are the three stations with takeoff angles farthest away from the steeply dipping nodal plane. The fits at the other stations deteriorate 15–20 s into the waveform. Several inversions were performed using different initial values for the depth and for the parametrization of the source time function, as well as for the weight of the CMT results. The focal mechanism, depth, and source duration were stable with respect to these perturbations, as were the more prominent features of the source time function, such as the rapid increase in moment release after approximately 4 s. The poor coverage of the focal sphere and the low signal-to-noise ratio prevents us from estimating the rupture direction and rupture speed from these data.

One important result is that the teleseismic P waveforms are consistent with the CMT focal mechanism and scalar moment. Even though we have data only from a small number of stations, these provide constraints on both the strike and dip of the steeply dipping plane. A very shallow dip for the second nodal plane therefore seems required for the overall focal mechanism (Table 1). The fact that this differs from our first-motion solution (compare the focal mechanisms in Figure 1 and Figure 4) can be explained in two ways: either the steeper dip of the first-motion mechanism is due to initial faulting on a steeper plane, while most of the moment release occurred on a more shallowly dipping plane (e.g., downdip rupture of a listric fault), or else the first-motion mechanism is incorrect by $\sim 10°$. It is clear, however, that a dip of 25° for the shallowly dipping plane would not be compatible with the teleseismic P wave data. A consequence of the agreement between the CMT mechanism and the P wave data is a better constraint on the scalar moment, which is sensitive to errors in the dip angle.

A second important result is the focal depth. We estimate that the depth of 9.7 km is associated with an error of 1 or 2 km. This is in good agreement with the depth estimate based on local travel time data (10.1 km), even though the depth determined from waveforms should be interpreted as an average depth for the entire rupture and source process.

Source Duration

The broadband teleseismic results show that the Kettleman Hills earthquake was an unusually slow event, in com-

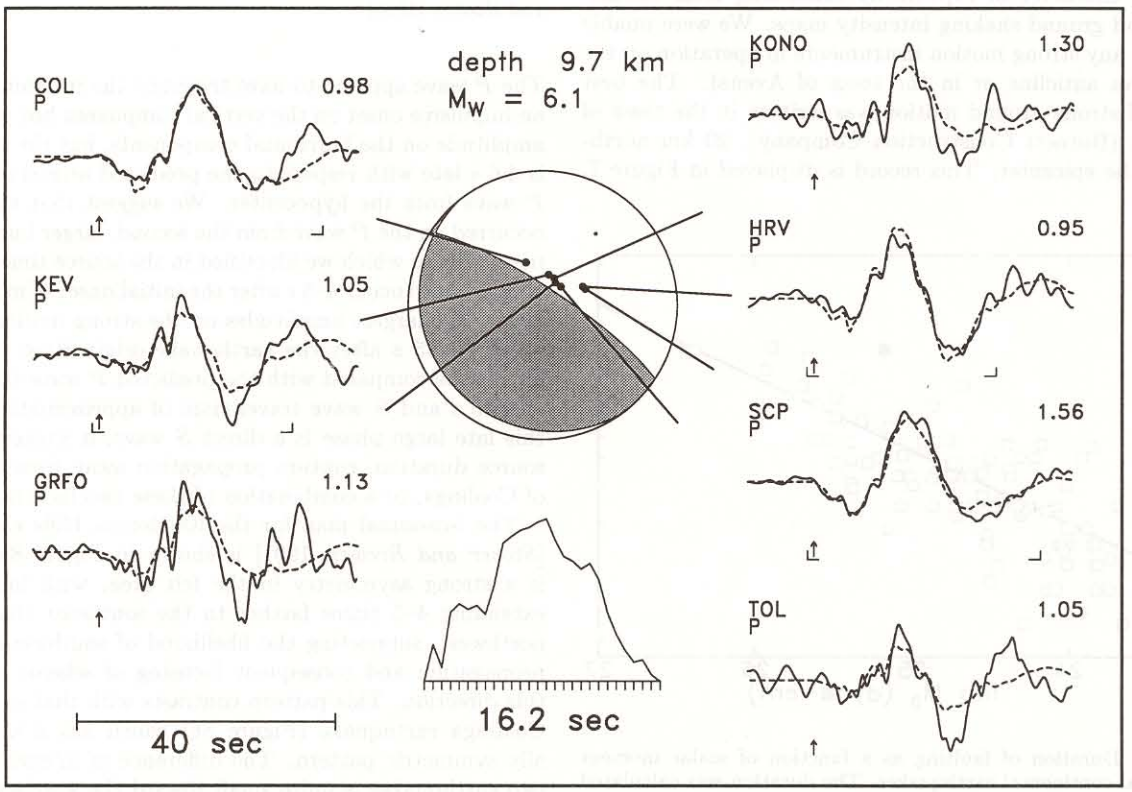

Fig. 5. Waveform inversion results for the Kettleman Hills main shock. Solid lines are the observed broadband waveforms, and dashed lines are the corresponding synthetic waveforms. The maximum amplitude is indicated in micrometers. The small arrow indicates the P wave arrival, and the brackets show the portion of the waveform that was used in the inversion (COL, KEV, HRV, and SCP only). The focal mechanism and the source time function are also shown.

parison with other continental earthquakes. The shape of the source time function (Figure 5) suggests that the earthquake initiated as a smaller shock which was followed approximately 4–5 s later by a more rapid rate of moment release. We compare the total duration of 16 s with those of other continental earthquakes analyzed using the same method and the same type of teleseismic data. The anomalous slowness of the Kettleman Hills earthquake is distinctive in Figure 6*a*, a plot of duration versus scalar moment for a large number of events in Asia [*Ekström*, 1987], the Aegean, North America, and Australia (G. Ekström, unpublished data, 1988). The data points show that the duration τ scales approximately with the scalar moment M_0 by

$$\tau = 2.0 \times 10^{-8} \times M_0^{1/3}$$

where τ is measured in seconds and M_0 in dyne centimeters. This is very similar to the global average relationship for moderate to large earthquakes and to the relationship obtained for shallow subduction zone events in the Aleutians [*Ekström and Engdahl*, 1989]. The relationship indicates that the average duration for an event with scalar moment 1–2 $\times 10^{25}$ dyn cm is 4–6 s. Conversely, a duration of 16 s is appropriate for an event with $M_0 = 5 \times 10^{26}$ dyn cm (M_W=7.1). Figure 6*b* shows a comparison of the rate of moment release of the Kettleman Hills (this study) and the 1983 Coalinga [*Hartzell and Heaton*, 1983] earthquakes. The two events exhibit very different rupture characteristics.

Strong Motion Recordings and Isoseismals

We sought independent observations of the source duration and character of rupture by examining local seismograms and ground shaking intensity maps. We were unable to locate any strong motion instruments in operation on the Kettleman anticline or in the town of Avenal. The best record of strong ground motion was written in the town of Coalinga (Burnett Construction Company), 20 km northwest of the epicenter. This record is displayed in Figure 7.

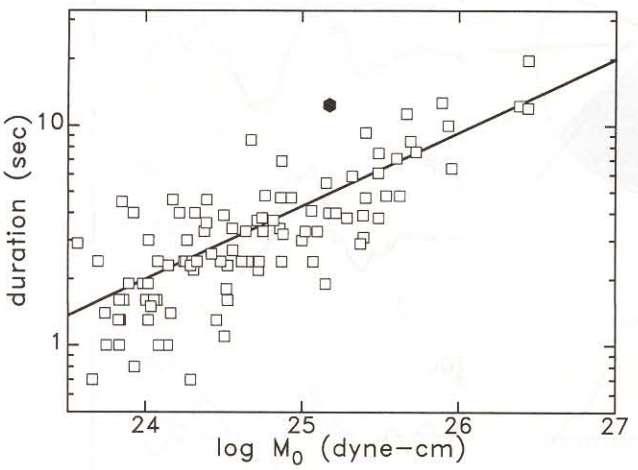

Fig. 6*a*. Duration of faulting as a function of scalar moment for several continental earthquakes. The duration was calculated from the source time function of each event as the shortest time over which 95% of the total moment was released. The solid hexagon corresponds to the Kettleman Hills earthquake, and the solid line to the relationship $\tau = 2.0 \times 10^{-8} \times M_0^{1/3}$ between duration τ (seconds) and scalar moment (dyne centimeters).

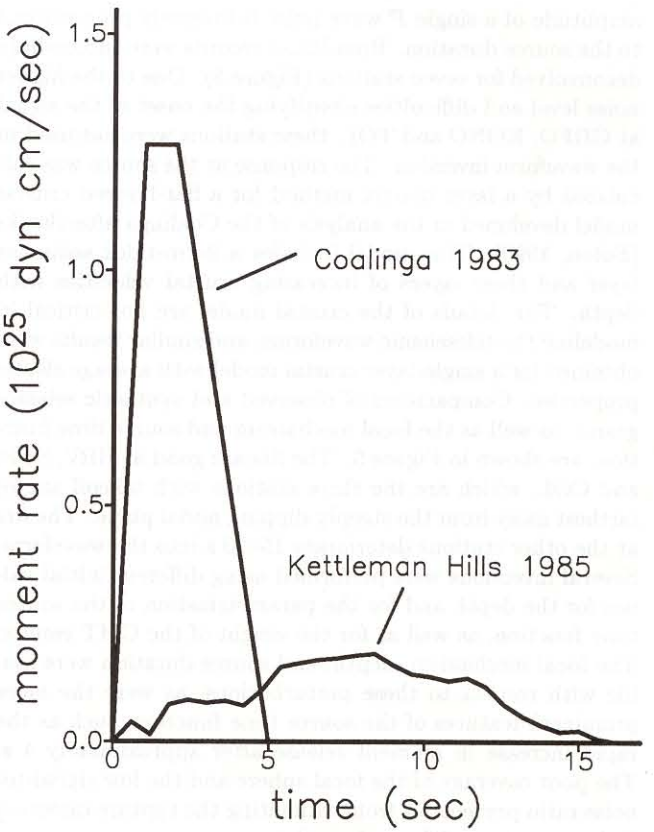

Fig. 6*b*. Comparison of the rate of moment release in the Kettleman Hills and 1983 Coalinga earthquake ruptures. The moment rate function for the Coalinga earthquake was taken from *Hartzell and Heaton* [1983]

The P wave appears to have triggered the instrument, with an impulsive onset on the vertical component but very small amplitude on the horizontal components, but the start time is 4.6 s late with respect to the predicted arrival of a direct P wave from the hypocenter. We suggest that the trigger occurred on the P wave from the second, larger burst of moment release which we identified in the source time function (Figure 5) to occur 4–5 s after the initial onset of moment release. The largest amplitudes on the strong motion records occur 20–25 s after the earthquake origin time. This delay can be compared with the predicted P wave travel time of 4.85 s and S wave travel time of approximately 8 s. If this late large phase is a direct S wave, it suggests a long source duration, rupture propagation away from the town of Coalinga, or a combination of these two factors.

The isoseismal map for the Kettleman Hills earthquake [*Stover and Brewer*, 1991] is shown in Figure 8*a*. There is a strong asymmetry in the felt area, with intensity V extending 4–5 times farther to the southeast than to the northwest, supporting the likelihood of southward rupture propagation and consequent focusing of seismic energy in this direction. This pattern contrasts with that of the 1983 Coalinga earthquake (Figure 8*b*) which has a more radially symmetric pattern. The difference in intensity for the two earthquakes is quite small toward the southeast, while the Coalinga earthquake was felt much stronger in other directions. The felt area for the Kettleman Hills earthquake is about 100,000 km^2 compared with approximately 250,000 km^2 for the Coalinga earthquake.

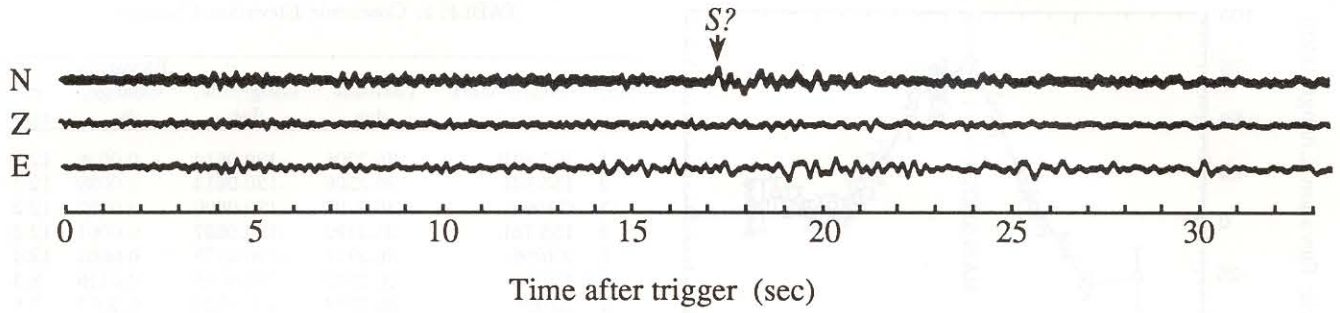

Fig. 7. Strong motion record written at Burnett Construction Company in the town of Coalinga.

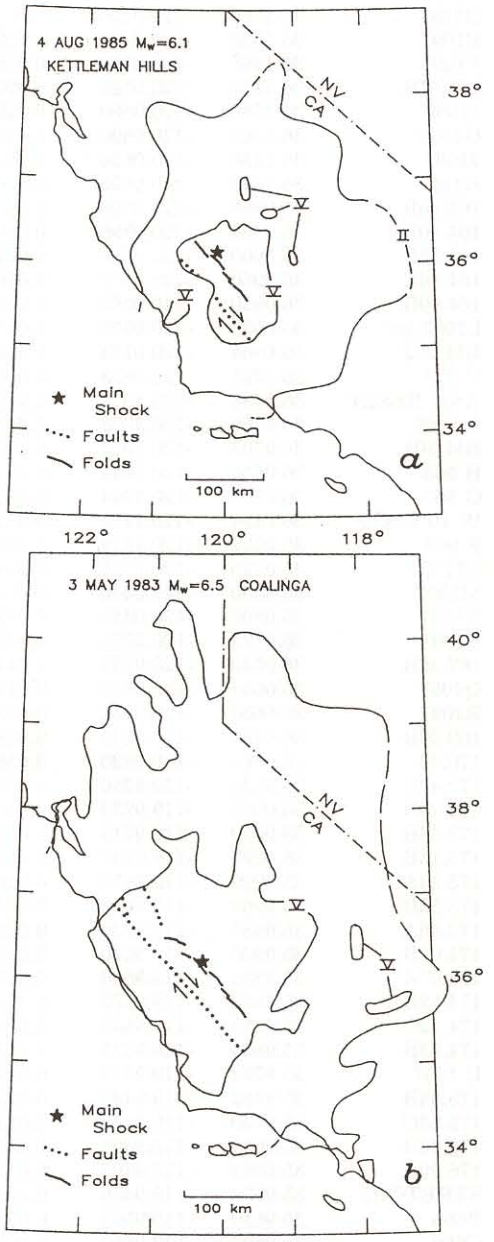

Fig. 8. Isoseismal maps for regions of modified Mercalli intensity V area and felt area (MM II) for (*a*) the Kettleman Hills earthquake [*Stover and Brewer*, 1991], and (*b*) the 1983 Coalinga earthquake [*Stover*, 1983]. Major faults and folds within the intensity V zone are shown. Southeastern direction of rupture propagation in 1985 is suggested by the asymmetrical intensity V zone.

STATIC DEFORMATION

A measure of the static deformation associated with the Kettleman Hills earthquake was obtained from resurvey of 70 bench marks in the vicinity of Kettleman North Dome (Figure 9). Precise (first-order) geodetic leveling was conducted in 1975 and 1989 by the National Geodetic Survey (NGS) and during 1978, 1982, 1983, and 1986 by the Department of Water Resources (DWR) of the State of California. In addition, several second- and third-order surveys by engineering firms were conducted during 1970–1985. The elevations of bench marks measured before the earthquake, during 1983–85, were subtracted from elevations measured after the earthquake, during 1986–1989, to deduce the "coseismic" or earthquake-associated elevation changes (Figure 10*a* and Table 2). An error analysis and corrections made to remove surveying errors and ground subsidence caused by water withdrawal are presented in the appendix.

Numerical Dislocation Experiments

We seek the fault geometry and slip compatible with the observed geodetic deformation (Table 2). A fault is simulated by superposition of point sources distributed uniformly over a rectangular surface at 1-km grid intervals and embed-

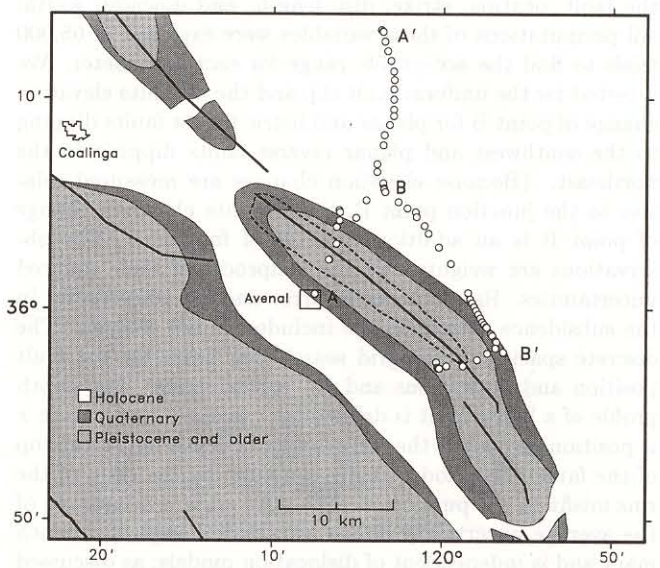

Fig. 9. Map of bench marks along the California aqueduct route (A′–B′), and along the Anticline crossing route (A–B). The Kettleman North Dome Oil field is outlined by the dashed line.

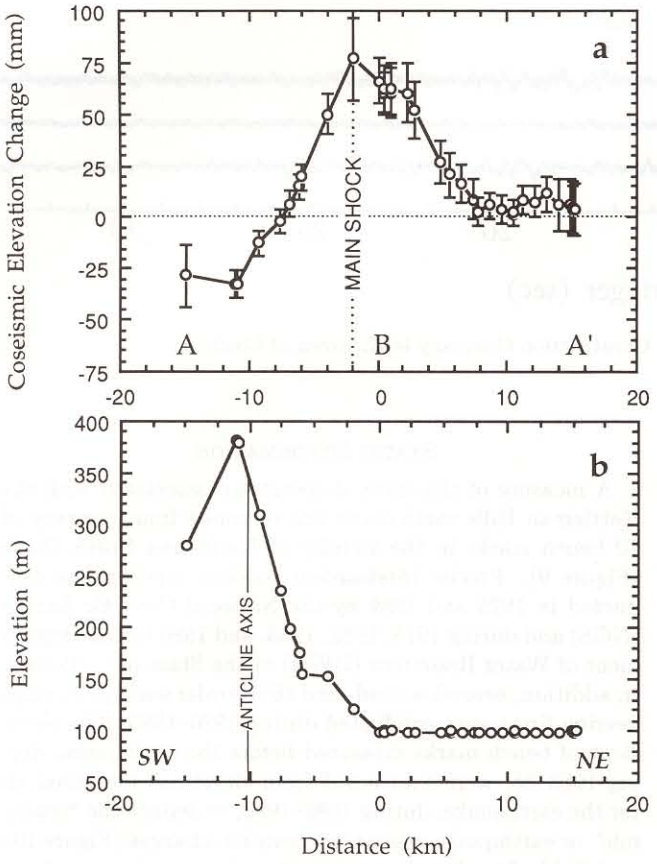

Fig. 10. Profiles of (a) coseismic elevation changes and their associated 1σ uncertainties, and (b) route topography nearly perpendicular to the anticline axis (A′–B–A). The town of Avenal is at km -12.

ded in an elastic half-space with Poisson's ratio 0.25 [*Barrientos et al.*, 1987]. Because the signal/noise ratio for the observed deformation is low (3.6), we restrict our search to uniform dip-slip motion on single rectangular faults. We tested a range of fault geometries by systematically varying the fault location, strike, dip, length, and downdip width. All permutations of these variables were explored in 65,000 trials to find the acceptable range for each parameter. We inverted for the uniform fault slip and the absolute elevation change of point B for planar and listric thrust faults dipping to the southwest and planar reverse faults dipping to the northeast. (Because elevation changes are measured relative to the junction point B, the absolute elevation change of point B is an additional degree of freedom.) The observations are weighted by the reciprocal of their squared uncertainties. Random survey error and the uncertainty in the subsidence correction are included in the weights. The discrete spacing in the grid search was 2 km for the fault position and dimensions and 10° for its strike. The depth profile of a listric fault is defined by $x = b_1 z + b_2 z^2$, where x is position normal to the strike and z is depth below the top of the fault. The model fitting is guided by the ratio of the rms misfit to the pure error. The pure error is a measure of the average uncertainty of the elevation change of a bench mark and is independent of dislocation models; as discussed in the appendix, it is 10.18 mm. Although we seek fault geometries with the lowest value of misfit/noise (M/N), we regard all models for which M/N $\leq$ 1.0 as acceptable. This

TABLE 2. Coseismic Elevation Changes

No.	Bench Mark	Latitude, deg	Longitude, deg	Elevation Change, m	σ, mm
1	155.64R	36.2206	-120.0614	0.0036	12.8
2	155.64L	36.2206	-120.0614	0.0039	12.1
3	G1098	36.2197	-120.0600	0.0052	12.2
4	155.78L	36.2192	-120.0597	0.0061	12.2
5	X1096	36.2117	-120.0578	0.0062	12.4
6	Y1096	36.2042	-120.0550	0.0116	8.3
7	Z1096	36.1964	-120.0519	0.0077	7.8
8	A1097	36.1881	-120.0492	0.0085	6.7
9	158.45R	36.1814	-120.0486	0.0024	6.5
10	158.47R	36.1814	-120.0486	0.0019	6.5
11	B1097	36.1740	-120.0490	0.0039	6.4
12	C1097	36.1660	-120.0490	0.0057	6.0
13	D1097	36.1580	-120.0490	0.0025	6.9
14	E1097	36.1530	-120.0490	0.0090	9.9
15	F1097	36.1460	-120.0530	0.0164	8.9
16	161.57R	36.1380	-120.0580	0.0208	10.9
17	J1098	36.1380	-120.0580	0.0206	11.1
18	G1097	36.1300	-120.0590	0.0268	10.8
19	J1097	36.1150	-120.0650	0.0523	13.9
20	K1097	36.1090	-120.0650	0.0602	14.2
21	164.40R	36.0990	-120.0590	0.0618	12.6
22	164.40L	36.1000	-120.0590	0.0604	11.9
23	164.68L	36.0960	-120.0580	0.0623	11.9
24	164.69L	36.0960	-120.0580	0.0598	10.3
25	164.69R	36.0950	-120.0580	0.0600	10.3
26	L1097-jct	36.0930	-120.0570	0.0658	10.9
27	BM 202	36.0864	-120.0753	0.0767	20.2
28	C 928	36.0725	-120.0853	0.0501	10.0
29	A806 RESET	36.0786	-120.1017	0.0198	6.3
30	L 1196	36.0769	-120.1008	0.0152	6.2
31	BM 204	36.0703	-120.1014	0.0064	6.1
32	H 963	36.0650	-120.1042	-0.0015	5.8
33	G 963	36.0517	-120.1044	-0.0125	6.2
34	W 10 USGS	36.0394	-120.1114	-0.0327	6.6
35	F 963	36.0392	-120.1119	-0.0324	6.6
36	CITY	36.0120	-120.1256	-0.0284	15.4
37	M1097	36.0850	-120.0440	0.0588	9.2
38	N1097	36.0800	-120.0350	0.0455	6.7
39	P1097	36.0770	-120.0270	0.0392	6.1
40	167.36R	36.0730	-120.0259	0.0443	8.4
41	Q1097	36.0660	-120.0180	0.0491	7.9
42	R1097	36.0600	-120.0140	0.0430	6.7
43	169.40R	36.0490	-120.0040	0.0398	7.8
44	170.42	36.0360	-119.9920	0.0380	8.5
45	172.40R	36.0130	-119.9750	0.0355	10.2
46	172.44B	36.0080	-119.9730	0.0301	9.4
47	172.58B	36.0050	-119.9710	0.0322	9.7
48	173.13B	36.0020	-119.9690	0.0290	11.4
49	173.13A	35.9990	-119.9670	0.0286	11.2
50	173.56B	35.9960	-119.9650	0.0229	11.1
51	173.56A	35.9930	-119.9630	0.0220	10.9
52	174.07B	35.9900	-119.9610	0.0192	10.0
53	174.07A	35.9880	-119.9590	0.0171	9.9
54	174.12B	35.9860	-119.9570	0.0194	9.8
55	174.12C	35.9855	-119.9565	0.0162	9.6
56	174.83B	35.9805	-119.9525	0.0142	9.9
57	U 1097	35.9790	-119.9510	0.0170	10.7
58	175.54B	35.9750	-119.9480	0.0228	13.6
59	175.54C	35.9740	-119.9470	0.0137	10.6
60	176.39B	35.9655	-119.9400	0.0072	10.2
61	176.39A	35.9660	-119.9405	0.0130	10.8
62	STRETCH2	35.9690	-119.9480	0.0082	9.6
63	B666	35.9650	-119.9560	0.0020	9.2
64	C666	35.9600	-119.9660	0.0078	9.6
65	D666	35.9550	-119.9800	0.0063	9.9
66	E666	35.9550	-119.9960	0.0041	10.1
67	R806	35.9580	-120.0060	0.0047	10.4
68	Z1159	35.9540	-120.0050	0.0020	10.5
69	Y1159	35.9530	-120.0040	0.0004	10.6
70	X1159	35.9530	-120.0030	0.0003	10.6

is because noise in the observations may influence the selection of the source parameters for models with M/N < 1.

We applied a depth correction to the elastic half-space results to account for the presence of compliant sedimentary rocks of the Great Valley sequence overlying stiffer Franciscan Complex and basement rocks. We simplified *Eberhart-Phillips*'s [1990] seismic velocity profile to a layer extending to a depth of 4.0–7.5 km with a P wave velocity v_P=3.5 km s^{-1} and density 2700 kg m^{-3} overlying a substrate with v_P=6.25 km s^{-1} and density 3000 kg m^{-3}; this yields a Young's modulus contrast of 3.5. The boundary between the upper and lower regions coincides with the 5.0 km s^{-1} contour of Figure 11. Using a two-dimensional boundary element model [*King and Ellis*, 1990], we found that the half-space solution underestimates the depth of the fault by 1.0 km for the reverse fault and 1.5 km for the thrust fault, because the low-modulus surface layer concentrates the surface deformation. The dip, slip, fault area, and moment do not change. These results are in qualitative agreement with findings of *Rodgers and Rizer* [1981] and *Reches and Zoback* [1990].

Dislocation Results

The deduced geodetic moment, M_0, is 0.9–2.3 × 10^{18} N m corresponding to a moment magnitude, 5.9 ≤ M_W ≤ 6.2 (Table 3). Both thrust faults dipping gently southwest and reverse faults dipping steeply northeast satisfy the observations (Figure 12). A shallow thrust fault (M/N=0.49, model 1 in Figures 11 and 12 and Table 3) fits the leveling data substantially better than a reverse fault (M/N=0.60; model 2). If one restricts the search to faults that pass within 2 km of the main shock hypocenter, reverse faults (M/N≥0.60) fit better than thrust faults (M/N≥0.78; model 3); M_W=6.0–6.2, and M_0=1.2–2.3 × 10^{18} N m. Since we consider all models for which M/N is acceptable, neither the thrust nor reverse faults can be rejected. It is also possible that slip occurred on parts of both planes.

The geodetic source parameters are in accord with the broadband seismic measure of the earthquake size (1.6 × 10^{18} N m), its strike (140°–160°) and dip (0–20°S with modest listric curvature permitted, or 60°–89°N; Table 3). Although the fault width (its downdip dimension) is poorly constrained (< 12 km), the length is found to be 22 ± 6 km, or nearly the full extent of the Kettleman Hills North Dome anticline. The main shock lies at the north end of the bottom of the model faults, suggesting that the rupture propagated both updip and southward (compare Figures 9 and 12).

An independent test of the geodetically determined moment can be made using the pressure changes measured in four water wells installed at depth of 10–24 m below the ground surface and continuously monitored by the USGS [*Roeloffs et al.*, 1989]. These wells recorded the coseismic static pressure changes (dilatations of 0.1–0.2 ppm) at a distance of about 35 km from the main shock. The wells have been calibrated by their response to barometric pressure changes and to the solid earth tides. The near-surface volumetric strains were calculated for the best fitting thrust and reverse faults constrained to pass near the main shock (from Table 1); the thrust fault, which fits the water well data best, is shown in Figure 13. The rms signal is 3.4 times larger than the misfit; the rms misfit to the model is 0.045 ppm. The lowest rms residuals (0.040 ppm) for the thrust model are obtained when the moment is reduced by 7%; M_0 = 1.16 × 10^{18} N m (M_W=6.0). Since the strains are proportional to the moment release, the water well observations offer independent support for the moment obtained from inversion of the leveling and seismic waveform data.

DISCUSSION

Where Is the Fault?

The dislocation experiments indicate that the distribution of aftershocks along strike (to the NW and SE), corresponds closely to the site of coseismic slip. Slip must terminate several kilometers north of the south end of Kettleman North Dome (Figure 13). However, aftershocks extend east of any geodetically acceptable fault model (Figure 11). In addition, aftershocks in the core of the anticline and those well to the SW cannot be associated with substantial fault slip. The Kettleman Hills earthquake shares with the Coalinga event

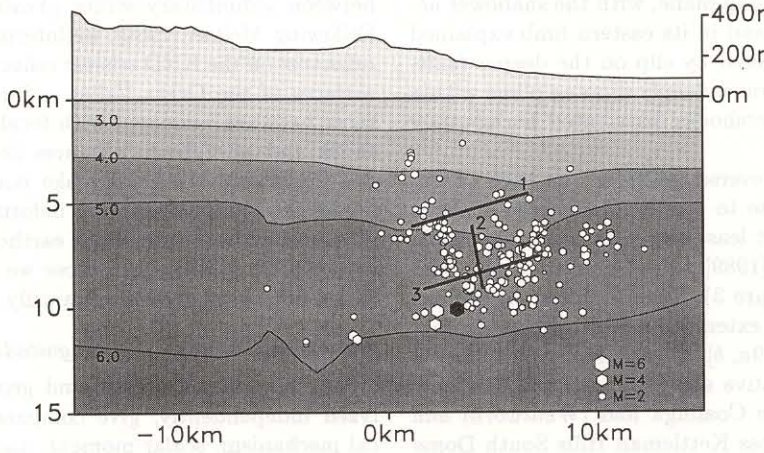

Fig. 11. Cross section through the main shock, showing the principal aftershocks and the profile of the best fitting fault (model 1) and the best fitting faults constrained to intersect the main shock (models 2 and 3). Thrust faults with some listricity would also fit the observations (Table 3). The viewing azimuth is 325°. The shaded background shows a cross section of the three-dimensional velocity model used in the relocation of the seismicity. The contour labels show the P wave velocity (km s^{-1}).

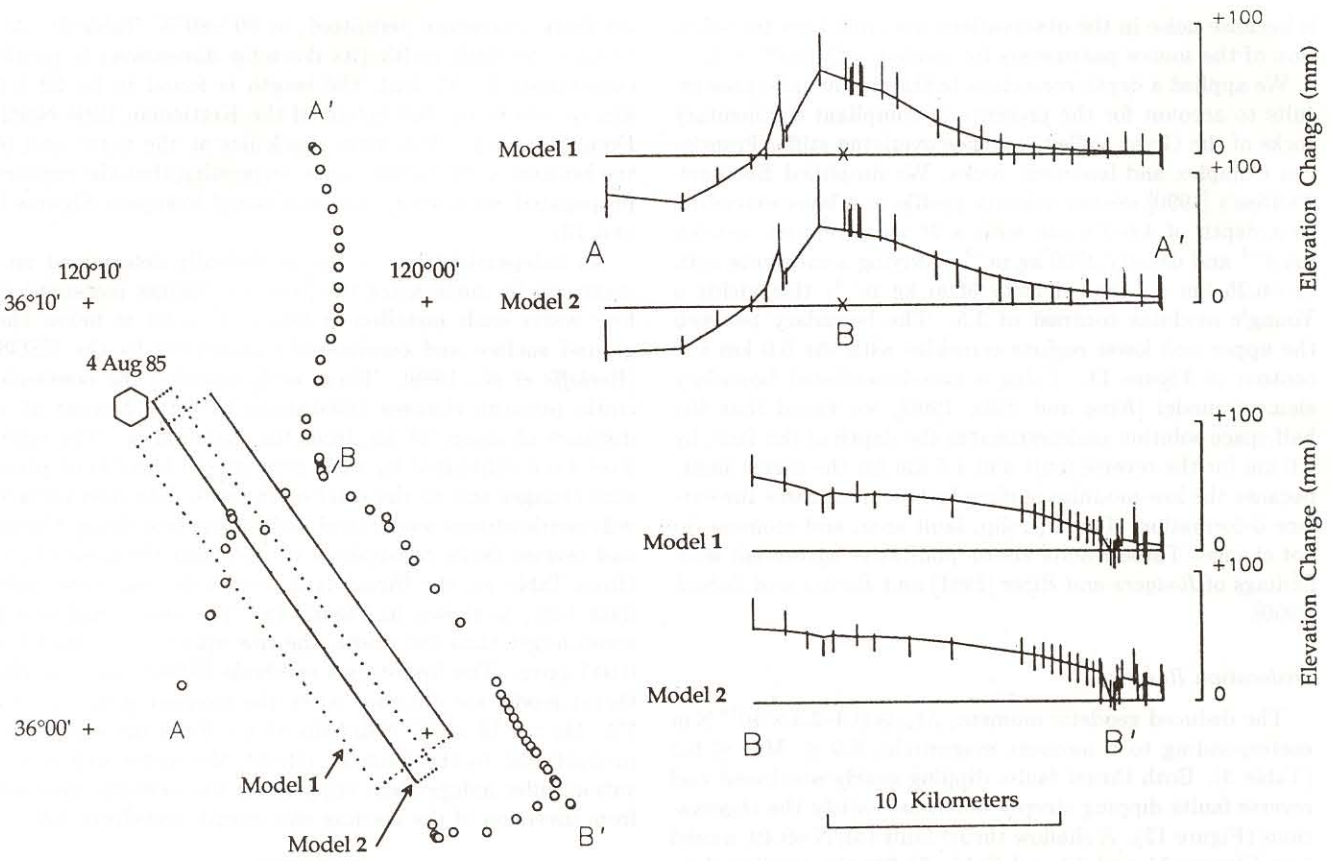

Fig. 12. The thrust fault which fits the observations best (model 1, Table 3), and the best fitting fault that intersects the hypocenter (model 2, Table 3). The faults are identified by the point sources along their perimeters; the upper edge is marked by a dashed line. The geodetic BMs are small circles. Profile A–A′ is projected onto an azimuth of 75°; profile B–B′ is projected along a 125° azimuth. The vertical lines are the observations and associated 1σ error bars; the model fit is shown by the line. The distance scale is the same for both map and profiles.

the property that in cross section, aftershocks are widely dispersed, making it difficult to determine which of the nodal planes is the fault plane. The observation that the aftershocks extend a large distance perpendicular to the fold axis and tend to be shallower beneath the eastern limb of the fold supports the shallowly dipping plane, with the shallower activity within the anticline and in its eastern limb explained as secondary faulting triggered by slip on the deeper fault. It is more difficult to envision a steeply dipping plane within the anticline triggering aftershocks distributed horizontally over a large area.

Small adjustments on reverse faults in the core of the anticline may be a response to slip on the master fault or faults at greater depth. At least one such high-angle fault is interpreted by *Meltzer* [1989] to be located in the core of the Kettleman fold (Figure 3). The Coalinga earthquake similarly shows aftershocks extending well into the anticlinal core [*Eberhart-Phillips*, 1989*a*, *b*]. Several high-angle reverse faults with modest cumulative slip are seen on the seismic reflection profile across the Coalinga fold [*Wentworth and Zoback*, 1989] and also across Kettleman Hills South Dome (R. Bloch et al., Style and magnitude of tectonic shortening normal to the San Andreas fault across Pyramid Hills and the Kettleman Hills South Dome, California, submitted to *Geological Society of America Bulletin*, 1992). Presumably such faults accommodate finite strains due to folding; fault slip in these shallower regions may be spatially separated from master faults at greater depth.

Several authors have proposed that the Coalinga earthquake [*Hill*, 1984] and other fold earthquakes are caused or accompanied by flexural slip, that is, slip on the interface between sedimentary strata [*Yeats*, 1986; *Rockwell*, 1988]. Following *Meltzer* [1989], we interpret the continuous bright reflectors on the KND seismic reflection profile to be bedding surfaces of the Great Valley sediments. When the dips of these beds are compared with focal mechanisms of the main shock and aftershocks (Figures 3*b* and 3*c*), no correspondence between the earthquake nodal planes and the beds are seen. Thus flexural slip deformation was either absent during the Kettleman Hills earthquake, occurred only for earthquakes smaller than those we determined focal mechanisms for, or occurred aseismically.

Earthquake Rupture and Magnitude

The broadband seismic and geodetic observations, analyzed independently, give comparable answers for the focal mechanism, scalar moment, and extent and direction of rupture for the Kettleman Hills earthquake. If we compare the teleseismic body wave magnitude (m_b=5.4) or the local magnitude (M_L=5.4–5.9) with the moment magnitude (M_W=6.1) determined from the broadband seismic analysis or the moment magnitude (M_W=6.0–6.2) calculated from

TABLE 3. Geodetic Modeling Results

Model[a]	Misfit/Noise Ratio	Moment, $\times 10^{18}$ N m	Magnitude M_W	Slip, m	Length, km	Width, km	Strike, deg	Dip or Listricity (b_1, b_2)[c]	Distance to Main Shock, km	Upper Depth, km	North Upper Corner,[d] km	North Upper Corner,[e] km
Thrust fault												
Best model (model 1, Figures 11 and 12)	0.49	1.01	6.0	0.24	22	6	145	15°S	4	4.5	19	25
Best constrained model[b] (model 3, Figure 11)	0.78	1.25	6.1	0.30	22	6	145	15°S	1.5	7.5	18	28
Acceptable range[b]	≤ 1.00	1.2–2.3	6.0–6.2	0.3–0.6	17–28	1–12	140–160	0–20°S (0.1–0.9,0.8–2.0)	0–2	7–11	18–20	25–29
Reverse fault												
Best model (model 2, Figures 11 and 12)	0.60	1.09	6.0	0.56	20	3	145	80°N	1.5	6	16	25
Acceptable range	≤ 1.00	0.9–2.3	5.9–6.2	0.23–0.7	16–28	3–10	140–150	60°–89°N	0–3	5–9	15–17	25–27

[a] All faults are rectangular surfaces with uniform dip-slip motion.
[b] Constrained faults intersect the main shock hypocenter (within ±2.0 km).
[c] Listric faults are defined by $x = b_1 \times z + b_2 \times z^2$, where x is the distance normal to the fault strike and z is the depth measured from the top of the fault.
[d] Distance measured east from −120.32°.
[e] Distance measured north from 35.90°.

the geodetic data, we observe that the short-period measurements of the seismic energy are much smaller than the long-period measurement. Indeed, if we use M_L to estimate the seismic moment using the moment magnitude relationship [*Hanks and Kanamori*, 1979], we obtain a moment which is a factor of 2–10 smaller than that determined from long-period seismic data. What, then, may have caused this low rate of moment release in the Kettleman Hills earthquake?

Using *Brune*'s [1970] scaling arguments for slip on a circular crack of radius R, and an average stress drop $\overline{\Delta\sigma}$, we have

$$M_0 = \frac{16}{7}\overline{\Delta\sigma}R^3$$

If we take the duration τ proportional to R (i.e., assuming constant rupture velocity), we get

$$\overline{\Delta\sigma} \propto \tau^{-3}$$

If the source duration for the Kettleman Hills earthquake is 2–4 times larger than other events of similar moment, this would suggest a stress drop 1/8 to 1/64 of the average event. However, simple scaling arguments would also lead to a 4–16 times larger than average rupture area, since the rupture area is proportional to R^2. Geodetic models of the rupture area range from 17 to 300 km^2 (Table 3). If we estimate the rupture extent from the horizontal extent of the aftershocks, we get a maximum area of approximately 200 km^2. This is not unusually large for an event of this scalar moment [*Kanamori and Anderson*, 1975], and the average static stress drop is therefore not anomalously low for the Kettleman Hills earthquake.

One way to produce a long source duration for a given source area and scalar moment is to introduce heterogeneities on the fault plane. If the fault plane is segmented into parts by offsets or strength heterogeneities (asperities or barriers) which do not break during the source process, the amount of moment release is less than in the absence of barriers [*Das and Aki*, 1977]. However, the unbroken barrier model (P-SV-1) of Das and Aki does not produce a slowdown of the rupture process. This is probably due to the simple geometry used by Das and Aki where the whole rupture front is blocked by the barrier. In a more realistic situation, the barriers could prevent parts of the rupture front from progressing and cause a complicated trajectory for the spread of the rupture. The unbroken patches on the fault plane restrain the amount of slip of the surrounding portions which do slip, and the total slip averaged over the whole fault area is also reduced. It is, however, not easy to reconcile such a model with another characteristic of the Kettleman Hills earthquake, its small number of aftershocks. If the rupture left many small patches unbroken in the main rupture, one could expect that many of these patches would fail subsequent to the main shock since they were stressed by the surrounding slip.

A second possible explanation for the slow rate of moment release is that faulting is occurring simultaneously on more than one fault plane, perhaps of different orientations. The diffuse aftershock pattern is consistent with such a model, but neither the 1982 New Idria or 1983 Coalinga earthquake (Figure 6*b*), which also had diffuse aftershock distributions, appear to have been unusually slow.

Fold Growth and Fault Slip Rates

Comparison of the geodetic and structural deformation affords a crude estimate of the growth rate of the Kettle-

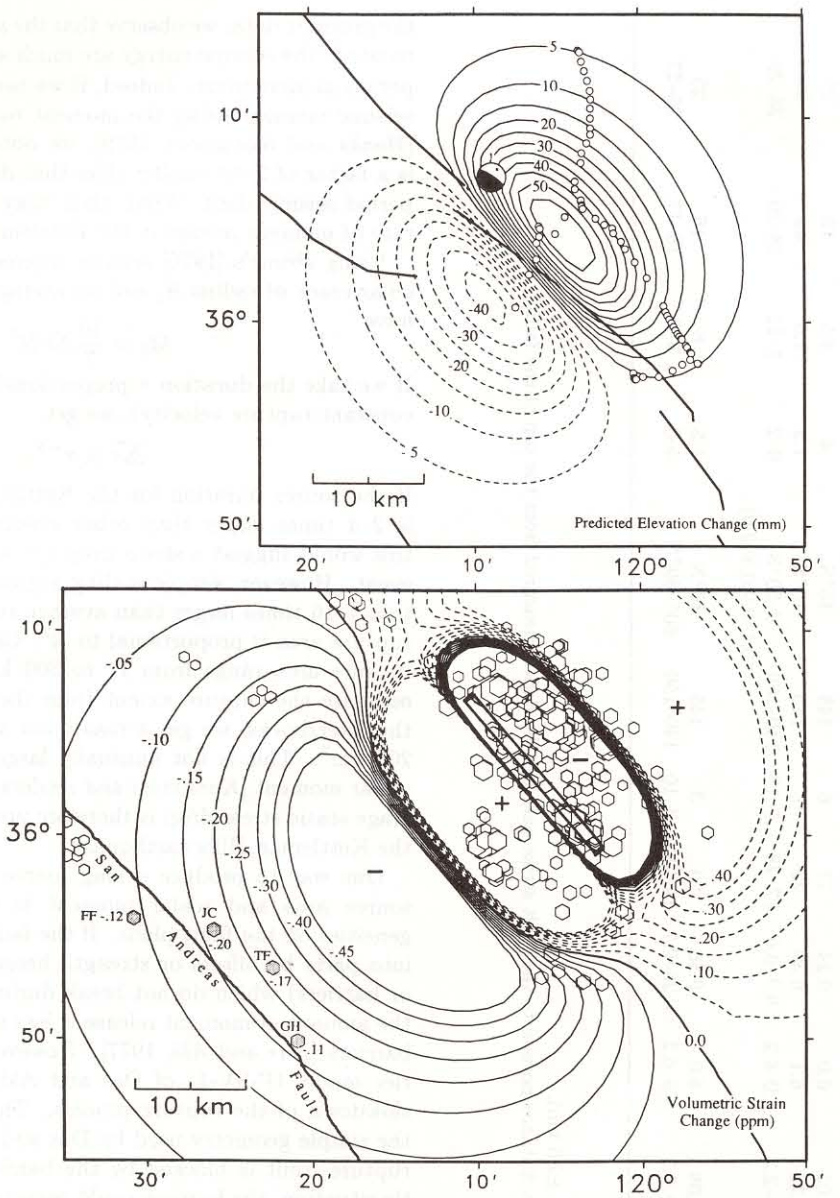

Fig. 13. Top map shows the vertical deformation field predicted for an acceptable thrust fault which intersects the hypocenter (Table 3) with the focal mechanism of the main shock. Lower map shows the near-surface volumetric coseismic strain change predicted for the same fault model, and the four labeled water wells from *Roeloffs et al.* [1989] used as dilatometers. The surface projection of the fault plane is shown by a rectangle.

man North Dome fold and the slip rate on the underlying fault. The structural relief on the north end of Kettleman North Dome is approximately 900 m based on the KND profile and associated well control (Figure 3*a*). This is consistent with *Zigler et al.*'s [1986] structure contour map on the Kreyenhagen Formation; *Namson and Davis* [1988] give 700 m for approximately the same location. From *Zigler et al.* [1986] it is evident that there is at least 1250 m of relief along the center of Kettleman North Dome. *Sarna-Wojcicki et al.* [1991] dated the Ishi tuff member of the Tuscan formation, immediately beneath the base of the Tulare formation on the east flank of Kettleman North Dome, at 2.4–2.6 Ma. *Obradovitch et al.* [1978] obtained a similar age for an ash deposit in approximately the same stratigraphic position on the anticline. Because the fold became active after deposition of the Tulare formation began [*Woodring et al.*, 1940, pp. 153–154; *Namson and Davis*, 1988, pp. 260–261], the fold can be no more than 2.5 m.y. old. Thus the long-term uplift rate is 0.43±0.07 mm/yr. Since the 7 cm of coseismic uplift was produced by 0.47±0.24 m of slip (Table 3), the long-term uplift rate corresponds to a fault slip rate of 2.9±0.6 mm/yr. Interseismic recovery of the coseismic uplift caused by asthenospheric or intracrustal relaxation will diminish this figure by as much as 50%.

CONCLUSIONS

We have shown that the Kettleman Hills earthquake occurred on a fault buried beneath a geologically young fold. The main shock and all well-constrained foreshocks and aftershocks exhibit compressional mechanisms perpendicular to the fold axis, suggesting that the fault undergoes pure dip-slip motion and accommodates contraction normal to

the San Andreas fault, which is oriented parallel to the fold and lies 30 km to the southwest. On the basis of aftershock locations, static deformation, teleseismic broadband analysis of the main shock, and seismic reflection data, the active fault appears to be a shallowly dipping thrust fault at a depth of 10 km beneath the fold. The main shock nucleated at, or in front of, the shallow tip of a fault imaged in seismic reflection profiles and several kilometers northeast of the fold axis. The pattern of geodetic uplift shows that most of the seismic slip occurred beneath the northeastern limb of the anticline, and the peak coseismic uplift is located 5 km northeast of the Quaternary fold axis. Unless subsequent earthquakes occur on the downdip extension (to the southwest) of the 1985 rupture, this suggests that the fold is propagating into the San Joaquin Valley.

Six foreshocks and the main shock locate at a single point, within the resolution of the data. The nucleation site is at the offset between the Kettleman Hills and Coalinga anticlines. Aftershock locations and geodetic uplift data show that the seismic rupture extended approximately 20 km southeast of this point. The rupture direction cannot be resolved in the teleseismic data, but the asymmetric pattern of isoseismal intensities is consistent with rupture propagation to the south. Thus a structural ramp or tear on the buried fault at depth controlled the pattern of large earthquake occurrence.

The diffuse pattern of aftershocks, with the shallowest events locating in the core of the anticline, cannot be ascribed to uncertainties in earthquake depth or position. Nor do the aftershocks result from flexural, or bedding plane, slip. We suggest that the pattern corresponds to secondary faulting on associated fractures and to small adjustments in the highly deformed and strained anticlinal cores. This pattern appears to be characteristic of compressional earthquakes on blind faults, such as the 1964 M_S=7.5 Niigata, Japan, earthquake [*Kawasumi*, 1973], the 1983 Coalinga, California, earthquake [*Eberhart-Phillips*, 1989*b*], the 1985 M_W=6.6, 6.8 Nahanni, Canada, events [*Wetmiller et al.*, 1988], and the 1987 M_W=6.0 Whittier Narrows, California, event [*Hauksson and Jones*, 1989].

The Kettleman Hills earthquake is highly unusual in its slow rate of moment release. The 16-s duration is more compatible with an earthquake 10 times bigger than the Kettleman Hills event. As a consequence, the source spectrum is depleted of energy at high frequencies, which has led to low local and body wave magnitude estimates with respect to the moment magnitude. This behavior is apparently not shared by the 1983 Coalinga earthquake. This points out that for earthquakes which deviate from standard source scaling relationships there is a large uncertainty in estimating scalar moments and slip or deformation rates from magnitudes determined from higher frequency seismic waves.

APPENDIX: LEVELING ERROR ANALYSIS

Random survey errors are proportional to the tolerances used in the surveys and propagate with the square root of distance. Random error assignments were thus based on the accuracy and internal consistency of each survey. Most sources of systematic error are slope or height dependent with proportionalities of 10–100 ppm; these include miscalibration of the graduated invar tapes suspended in the leveling rods, thermal expansion and contraction of the tapes, and atmospheric refraction of the line of sight between the instrument and rods. Because the majority of the surveying was conducted along the California aqueduct (route A′–B′, Figures 9 and 10), where the height difference across the network was just 9 m, the associated effects are smaller than random error. The short segment that traverses the anticline (route A–B, Figures 9 and 10) shows no correlation between height and the observed elevation change, indicating that these errors are also small over the anticline (compare Figures 10*a* and 10*b*). We did, however, find large errors in the DWR surveys caused by the use of Zeiss Ni1 automatic leveling instruments, which required correction.

Magnetic Errors

One of the principal automatic-compensating leveling instruments in use throughout the world, the Zeiss Oberkochen Ni1, had a design defect that caused the compensator, which acts as a plumb bob to align the optics horizontally, to be deflected toward magnetic north. Other automatic (or self-leveling) instruments also suffer from such an error, but to a lesser degree. Such errors were first reported by *Rumpf and Meurisch* [1981] and have since been extensively tested in NGS leveling by *Packard and MacNeil* [1983], *Strange* [1985] and *Holdahl et al.* [1986]. Although we were able to determine where the seven DWR instruments were used, only one was available for field testing and calibration. The original compensators for most instruments have been replaced, or the instruments were lost or stolen. We therefore sought to remove the errors by finding the magnetic coefficient for each instrument that minimized the observed differences in elevation between the error-free NGS surveys conducted in 1975 and 1989 and each of the four intervening DWR surveys. We were able to make reliable assessments for four instruments, resulting in corrections of 0.0–4.5 mm km^{-1}; three instruments were used so sparingly that we could deduce only that the errors were less than 1.0 mm km^{-1}. The corrections chiefly affect the aqueduct leveling (segment A′–B′ in Figure 9). A 1989 field test of the one DWR instrument used on the anticline-crossing route in 1983 showed that its error was less than 0.6 mm km^{-1}.

The magnetic susceptibility b of each instrument is different. The error is cumulative and is proportional to the vector component of the earth's local magnetic field in the direction of the optical axis (or line of sight) of the instrument. Thus the error per pair of bench marks (BMs) is

$$bM \cos\xi \cos(\phi - \psi)L$$

where M is the intensity of the magnetic field in gauss, L is the distance between the two BMs, ξ is the inclination, and ϕ is route azimuth between the pair of BMs and ψ the declination of the magnetic vector. This error is summed along the route. Since $M \cos\xi$ is 0.253 G over the Kettleman network, only ϕ varies more than a negligible amount over the 50 km span of the BMs, and thus the error can be expressed as the product of an instrument coefficient a, where $a = bM \cos\xi$, and $\sum_i \cos(\phi_i - \psi)L_i$, a function which accumulates with distance along the aqueduct from a reference bench mark, as shown in Figure A1.

The observed elevation changes are shown in Figure A2*a*. Note that the profiles exhibit little elevation change near B (km 20) and from B′ to the south (km 40–50). The leveling route is nearly perpendicular to magnetic north at these locations (see Figure 9), and thus little magnetic error accu-

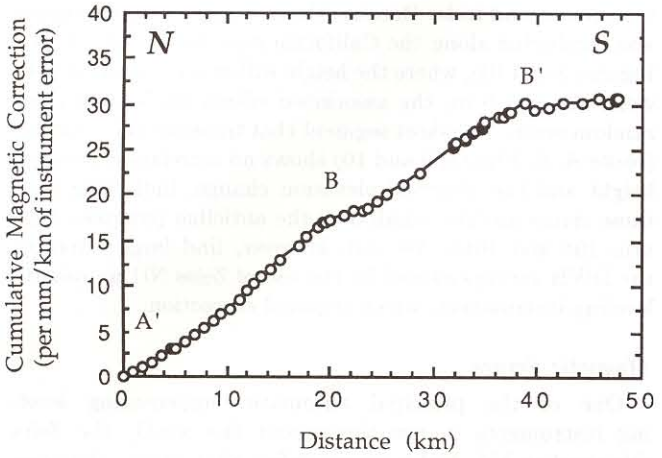

Fig. A1. Magnetic error as a function of distance along the aqueduct route. Note that the error diminishes to the south where the leveling route runs west across the anticline.

mulates there. This is confirmed by inspection of Figure A1, which shows negligible error accumulation near B and south of B′. The profiles for 1975–1978 and 1978–1982 are roughly mirror images of each other, as are the profiles for 1982–1983, and 1983–1986 (the coseismic interval). This suggests that the largest errors occurred during the 1978 and 1983 surveys. Note that the form of the magnetic error curve in Figure A1 will be found in the observed elevation changes in Figure A2*a* only if instruments were not changed along the route and if nontectonic subsidence was modest. Instrument usage is charted in Figure A3. Most of the 1978 survey was carried out with DWR Nil 71129, and all of the 1983 survey was conducted with DWR Nil 701611. In contrast, several instrument changes were made during the 1982 and 1986 surveys.

We found the instrument coefficient a that minimized the elevation changes between successive pairs of surveys, and between each survey when differenced with the error-free 1989 NGS surveys and a NGS 1975 survey that the NGS subsequently corrected for magnetic error of 0.83 mm km^{-1} [*Holdahl et al.*, 1986]. This method yields the smallest possible coseismic elevation change and also the smallest subsidence corrections. Comparison of the 1975 and 1989 surveys (not plotted) showed that no long-term elevation changes occurred between the north and south end of the lines, suggesting that the method is appropriate. Errors less than 0.5 mm km^{-1} could not be resolved because of competing sources of noise. A single coefficient is assigned to each instrument. Since in two cases, the same instrument was used in more than one survey, the consistency of the correction supplies one test for the fidelity of the correction. One such test succeeded (Nil 107287) and one failed, for Nil 71129 exhibits a different coefficient during 1978 and 1986. Inquiries with its owner, DWR-Sacramento, revealed no information to substantiate the change, such as replacement of the compensator, or known remagnetization of the instrument between 1978 and 1986. Remagnetization can occur when the instrument is passed through a powerful electromagnetic field, such as in the vicinity of high-voltage power lines. We have treated Nil 71129 as if it was remagnetized between 1978 and 1986.

Once the coefficients shown in Figure A3 are applied to the instruments, successive profiles of elevation change show no mirror images, and the patterns of elevation change for all but the coseismic period (1983–1986) are similar (see Figure A2*b*). These results suggest that most of the errors

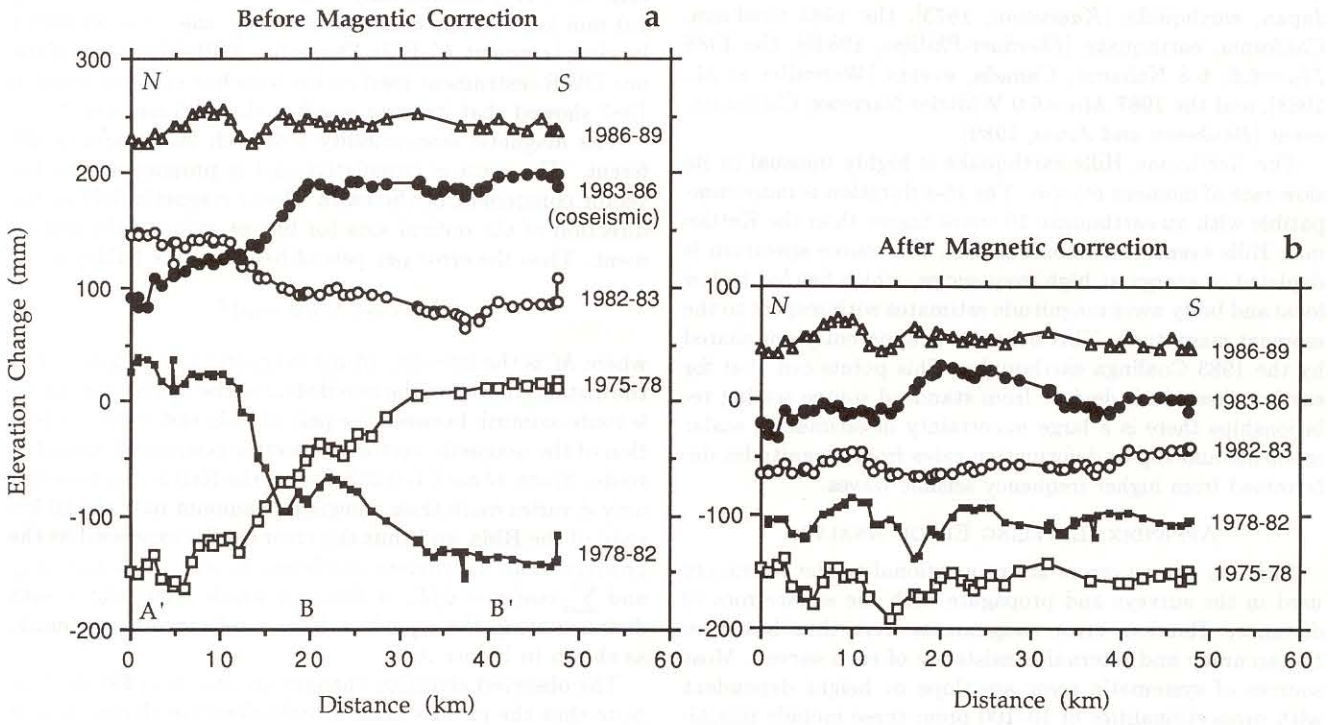

Fig. A2. Successive profiles of elevation change (chronologically, bottom to top) along the aqueduct route (*a*) before and (*b*) after correction for magnetic error. Nontectonic subsidence tends to be concentrated roughly at km 15 and km 38.

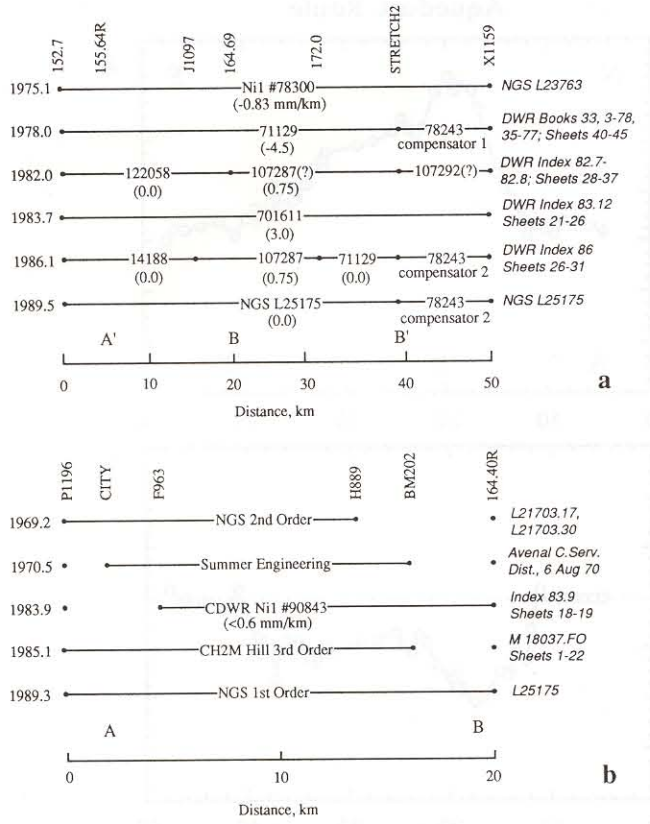

Fig. A3. Chart showing the Line numbers, leveling instrument and applied coefficients on (*a*) the anticline and (*b*) aqueduct routes.

attributable to magnetic compensators have been removed from the aqueduct leveling. We did find mirror image profiles with amplitudes of less than 10 mm for pairs of surveys that were not successive. For example, 1978–1983 and 1986–1989 profiles (not plotted), mirror each other at a distance of 15–50 km, but no instruments are in common over this range. We suspect that these patterns indicate residual errors that cannot be ascribed to magnetic instruments or other known sources, which we have not successfully removed.

One DWR instrument (Ni1 90843) was used on the northern half of the anticline route. In 1989 the DWR-Santa Nella conducted a 30-km-long survey of a segment of the aqueduct which had been surveyed by the NGS in 1975. Comparison of the 1989 DWR elevations with the error-free 1975 survey reveals that the coefficient for Ni1 90843 must be less than 0.6 mm km^{-1} (Figure A4). Since this is within the random error propagation, we have made no correction for this DWR instrument.

We also found what we believe to be a blunder in one section of the 1978 survey (BMs F1097–161.57R, 0.96 km apart, at km 14 in Figure A2*b*). Here the elevation difference between the BMs measured in the forward direction exceeded that measured in the backward direction by the 3-mm tolerance for the first-order survey and was rerun. The rerun section greatly exceeded the tolerance in both of the original differences, and should have been rerun again, but the crew instead averaged the two original differences to calculate the elevation difference and rejected the rerun, an impermissible procedure in first-order leveling. We therefore substituted the 1983 difference for these BMs for the 1978 difference, a correction of 12 mm.

Subsidence Correction

To isolate the deformation attributable to the earthquake, nontectonic subsidence must be removed from the coseismic elevation changes. Subsidence occurs in the eastern margin of the San Joaquin Valley because of pumping of aquifers for groundwater [see *Bull*, 1975]. Although the rate of subsidence has diminished sharply since 1970, when the aqueduct replaced pumping as the principal source of water for irrigation, subsidence rates of up to 15 mm yr^{-1} were measured in the network during 1980–1982. Pumping of the anticline for oil and gas also causes subsidence over Kettleman North Dome, amounting to less than 5 mm yr^{-1} over the oil field during 1970–1985. Once the magnetic errors were removed, we used the subsidence rate measured during the decade before the earthquake and the record of water, gas, and oil pumping to correct for the pumping-induced subsidence (Figure A5). Implicit in this correction is an assumption of constant subsidence rate from 1981 through 1986, whereas we know only that it was nearly constant during the overlapping interval, 1977–1983. Any tectonic deformation that occurred during the 22 months before the earthquake or during the 6 months (and for a limited segment, 44 months) following the earthquake is included as "coseismic."

Aqueduct route. The coseismic period spans 2.4 years (1983–1986) for the aqueduct leveling; for the anticline leveling it spans 4.2–5.4 years (1983/1985–1989). We used the deformation rate measured before the earthquake to correct the coseismic interval. Sources of nontectonic deformation (chiefly subsidence) are pumping of aquifers in the San Joaquin Valley and Kettleman Plain for groundwater and pumping of oil, water, and gas beneath the anticline. The water table in the vicinity of the aqueduct declined at a rate of 2–3 m yr^{-1} until about 1970, after which aqueduct deliveries of water replaced groundwater pumping and the water table began to rise at 3–4 m yr^{-1} (Figure A6*a*). The long-term rate of subsidence at B (BM L1097) is shown in Figure A6*b*. The subsidence rate diminished from about 100 mm yr^{-1} before the aqueduct was installed in 1970 to 10

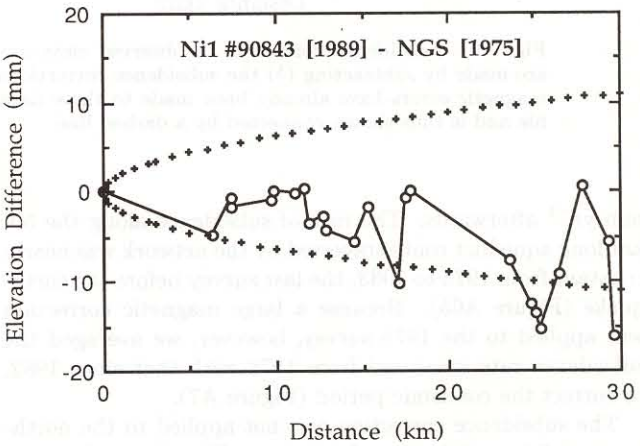

Fig. A4. Comparison of 1989 survey by the DWR using Zeiss Ni1 90843 against NGS leveling performed in 1975 along Mile 9–37 of the California aqueduct. No magnetic error can be discerned above the random error envelope (dashed parabola).

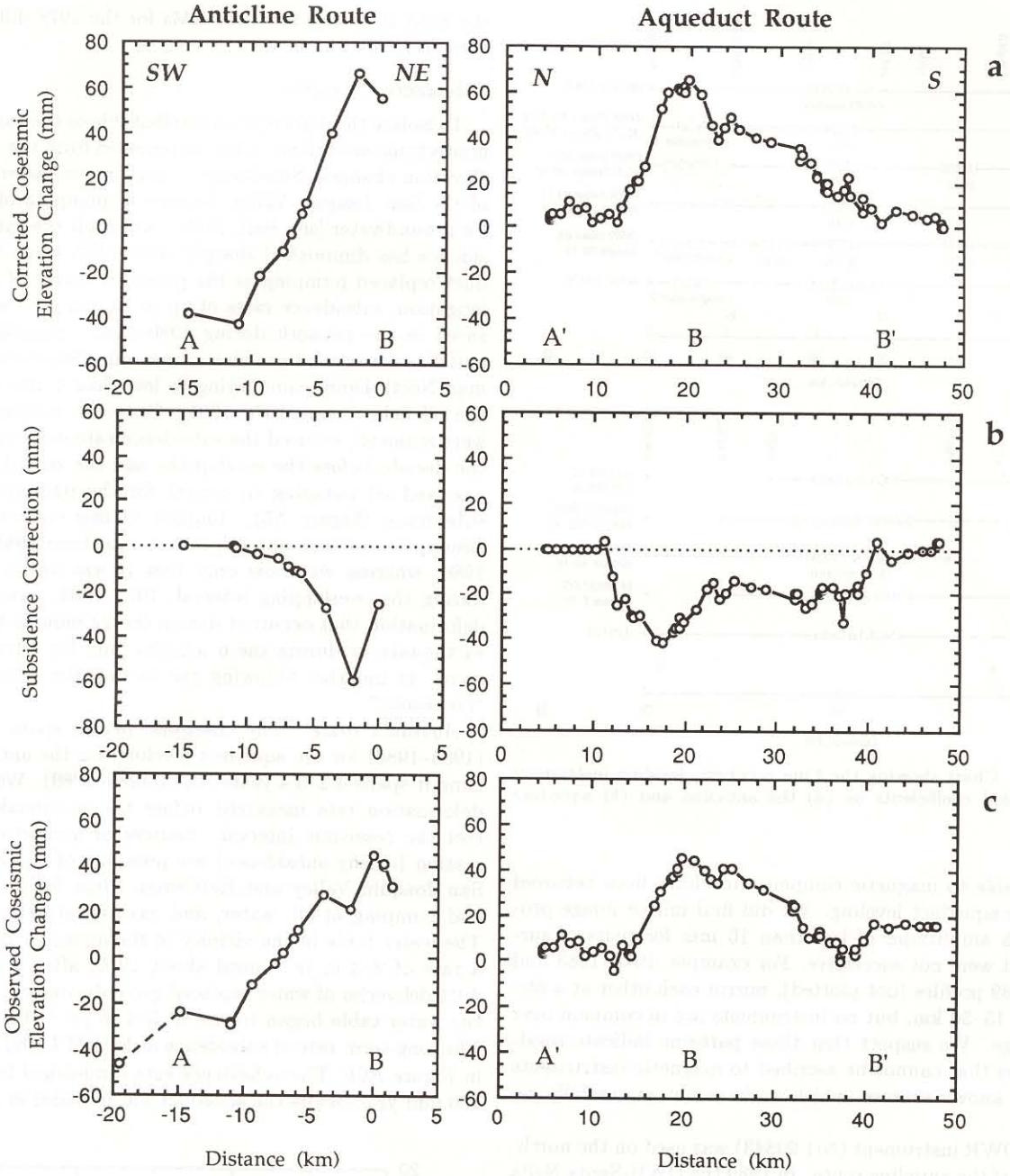

Fig. A5. Subsidence correction to observed elevation changes. (*a*) The corrected coseismic elevation changes are made by subtracting (*b*) the subsidence corrections from (*c*) the observed coseismic changes. Corrections for magnetic errors have already been made to these data. BM P1169 at km -20 was not retained in the coseismic file and is thus shown connected by a dashed line.

mm yr^{-1} afterwards. The rate of subsidence along the 50-km-long aqueduct route traversed by the network was nearly constant from 1978 to 1983, the last survey before the earthquake (Figure A6*b*). Because a large magnetic correction was applied to the 1978 survey, however, we averaged the subsidence rate measured from 1978 with that since 1982, to correct the coseismic period (Figure A7).

The subsidence correction was not applied to the northernmost 7 km of the aqueduct route. The observed coseismic elevation changes (before subsidence correction) exhibit no deformation along the northern 10 km of the aqueduct route (km 5–15 in Figure A7*b*), whereas the subsidence rate there during 1978–1983 was large (km 5–15 in Figure A7*a*). Applying the correction to the northern 7 km produces the dashed profile in Figure A7*b*. A test of the success of a subsidence correction is that short-wavelength deformation seen in the observed elevation changes should be reduced. This can be seen in the segment at km 30–45, where a subsidence trough disappears after correction. In contrast, the correction adds fluctuations at the north end where no relative subsidence is seen in the observed data. We were unable to obtain water table data for the period 1978–1986 at the north end and thus do not know whether subsidence diminished during 1983–1986. We have left the north end of

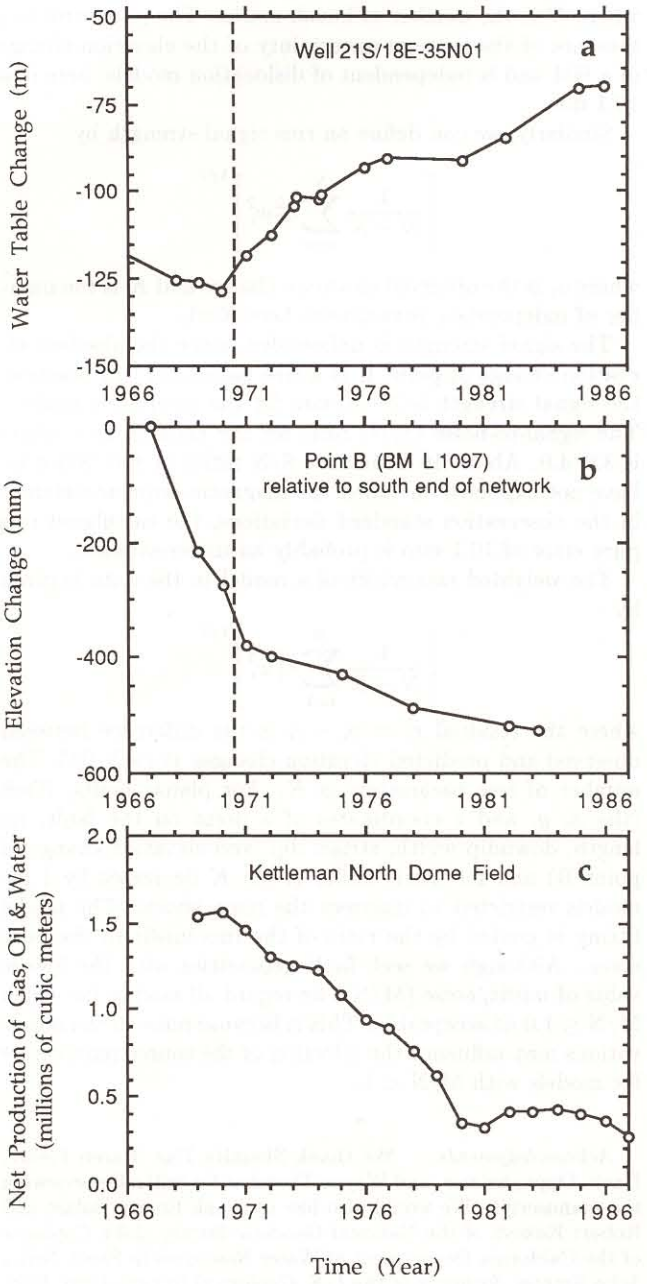

Fig. A6. (*a*) Depth from the ground surface to the water table at USGS observation well 21S/18E-35NO1, located on the aqueduct 7 km south of point B at km 27. Aquifers have been recharging since about 1970, when deliveries from the California aqueduct largely replaced pumping. (*b*) Subsidence history of BM L1097 (point B in profiles and route map) relative to south end of network, BM X1159, atop the anticline. Note that subsidence continues at one tenth its former rate. (*c*) Net production of gas, oil, and water for the Kettleman North Dome field [*Conservation Committee of California Oil Producers*, 1974–1987]. Both gas and liquid production have slowed since 1980.

the line uncorrected for subsidence (from BM D1097 north to 155.64R), weighting this segment to reflect added uncertainty in these elevation changes in the model fitting.

Anticline route. The anticline route contains one segment subject to pumping for groundwater (km 0 to km -7, left panel in Figure A5*b*), and one segment that traverses the oil field (km -7 to km -11). Since the subsidence rate near the aqueduct has been uniform since about 1970 (Figure A6*b*), we used the rate of subsidence measured between 1970 and 1983 to correct the observed coseismic elevation changes (principally 1983–1989) over the range km 0 to -7. We could not use the 1983–1985 preseismic elevation changes for the correction because the 1985 survey was conducted at low precision (third order) and did not occupy all of the BMs surveyed in 1983. The 17 mm yr^{-1} subsidence rate for BM 202 (located at km -2 in Figure A5), the highest for the network, was confirmed, however, by the 1983–1985 rate. The subsidence rate for BM C928 (at km -4 in Figure A5) was interpolated, since the BM was not observed in 1970 or 1985. Coseismic elevation changes for the five BMs near point B that were occupied in both 1986 and 1989 agree within 4 mm, suggesting that the correction is effective.

The cumulative oil, gas, and water volume withdrawn from the oil field during 1983–1989 (the coseismic period) is 22% of that withdrawn during 1970–1983 (the preseismic period), as can be seen in Figure A6*c*. The producing zones (principally the Temblor Miocene sands) are 1.9–2.5 km deep. Thus the subsidence associated with removal of fluids should diminish to modest amounts within several kilometers of the edge of the field [see *Segall*, 1985]. Thus 0.22 times the preseismic subsidence was applied as the subsidence correction within 2 km of the oil field.

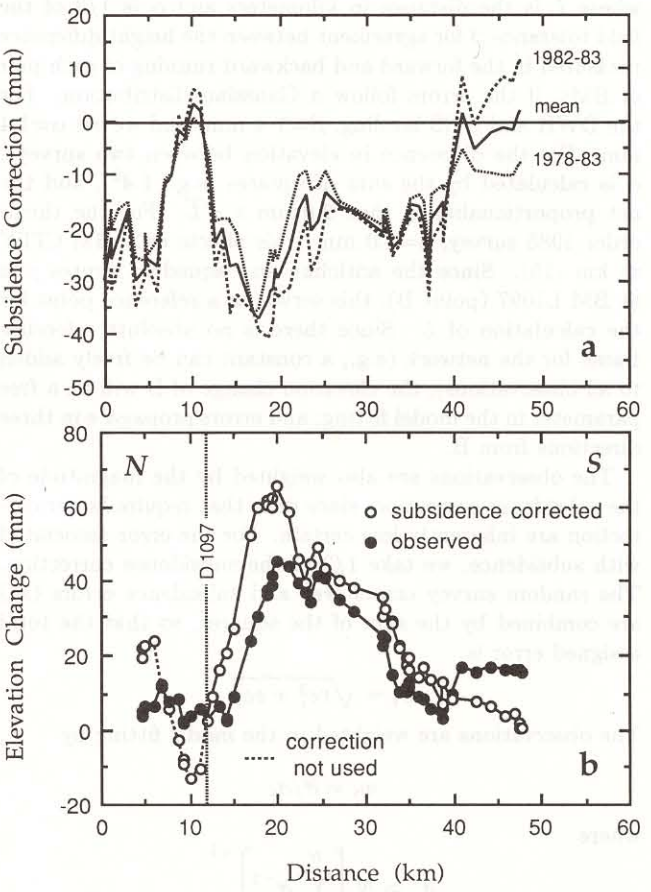

Fig. A7. (*a*) Subsidence correction to coseismic period for the aqueduct route. The mean rate between 1978-1983 and 1982-1983 was used to minimize the impact of any individual magnetic error assignment. (*b*) The observed and subsidence corrected coseismic elevation changes along the aqueduct route. Corrections north of D1097 (4–12 km) were not used since the observed elevation changes show no relative subsidence.

The westernmost BM in the network (BM CITY at point A in Figures 9, 10, and A5) was surveyed in 1985.1 and 1989.5. We have no information on its subsidence history, but since it is 2.5 km southwest of the oil field and located on the flank of the anticline outside of the alluvium subject to pumping for groundwater, we have made no subsidence correction to it. One BM (P1196 at km -20 in the left panel of Figure A5*b*) located 5.7 km south of CITY was surveyed in 1969, 1985, and 1989. The preseismic subsidence rate for P1196 is unknown. P1196 is the only BM in the network located west of the anticline in the Kettleman Plain. Despite an extensive records search, the only independent information we have to assess subsidence in the plain is one well, 22S17E-26H01, located 2.4 km ENE of P1196, which was measured when drilled in 1972 and again in 1987 and 1988. It showed a water table decline at a rate of 0.3 m yr^{-1}, indicative of pumping. This information, taken together with the low precision of the 1985 survey, has led us to omit the BM from the model fitting.

Assignment of Errors to the Coseismic Observations

Random survey error, re, is proportional to the square root of distance from a reference BM,

$$re = \alpha\sqrt{L}$$

where L is the distance in kilometers and α is 1/3 of the field tolerance β for agreement between the height difference measured in the forward and backward running of each pair of BMs, if the errors follow a Gaussian distribution. For the DWR and NGS leveling, β=3–4 mm, and we set α=1.4 mm. For the difference in elevation between two surveys, α is calculated by the sum of squares (e.g., 1.4^2), and the net proportionality is thus 2.0 mm $\times \sqrt{L}$. For the third-order 1985 survey, α=4.0 mm (this affects only BM CITY at km -15). Since the anticline and aqueduct routes join at BM L1097 (point B), this serves as a reference point for the calculation of L. Since there is no absolute reference frame for the network (e.g., a constant can be freely added to all observations), the elevation change of B will be a free parameter in the model fitting, and errors propagate in three directions from B.

The observations are also weighted by the magnitude of the subsidence correction, since data that require larger correction are inherently less certain. For the error associated with subsidence, we take 1/3 of the subsidence correction. The random survey errors (re) and subsidence errors (se) are combined by the sum of the squares, so that the total assigned error is

$$\sigma_i = \sqrt{re_i^2 + se_i^2}$$

The observations are weighted in the model fitting by

$$w_i = \overline{\sigma}/\sigma_i$$

where

$$\overline{\sigma}^2 = N\left[\sum_{i=1}^{N} \sigma_i^{-2}\right]^{-1}$$

is the mean variance and N is the number of observations (here, N=70). The weighted rms pure error is

$$\left[\frac{1}{N}\sum \sigma_i^2\right]^{1/2}$$

where N is the number of bench marks. The pure error is a measure of the average uncertainty of the elevation change of a BM and is independent of dislocation models; here it is 10.1 mm.

Similarly, we can define an rms signal strength by

$$\left[\frac{1}{N-K}\sum_{i=1}^{N} o_i^2 w_i^2\right]^{1/2}$$

where o_i is the observed elevation change and K is the number of independent parameters; here K=1.

The signal strength is unbounded, since the absolute elevation change of point B is a free parameter. In practice, the signal strength is 25–30 mm for the acceptable models. The signal-to-noise (S/N) ratio for the network as a whole is 3.0–4.0. About 10 BMs have S/N ratios of 4–6. Since we have not explicitly included the magnetic error uncertainty in the observation standard deviations, the calculated rms pure error of 10.1 mm is probably an underestimate.

The weighted rms misfit of a model to the data is given by

$$\left[\frac{1}{N-K}\sum_{i=1}^{N} r_i^2 w_i^2\right]^{1/2}$$

where the residual $r_i = o_i - c_i$ is the difference between observed and predicted elevation changes at each BM. The number of free parameters is K. For planar faults, K=8 (the x, y, and z coordinates of a point on the fault, its length, downdip width, strike, dip, and elevation change of point B) and for listric faults K=9; K decreases by 1 for models restricted to intersect the main shock. The model fitting is guided by the ratio of the rms misfit to the pure error. Although we seek fault geometries with the lowest value of misfit/noise (M/N), we regard all models for which M/N $\leq$ 1.0 as acceptable. This is because noise in the observations may influence the selection of the source parameters for models with M/N $<$ 1.

Acknowledgments. We thank Shamita Das, Karen Fisher, David Oppenheimer, and Wayne Thatcher for critically reviewing the manuscript. We would also like to thank Emery Balazs and Robert Kokesh of the National Geodetic Survey, John Coplantz of the California Department of Water Resources in Santa Nella, John Estrem, formerly of the U.S. Geological Survey, Gary Dobson of CH2M-Hill Engineering in Sacramento, and Joseph McGahan of Summers Engineering in Hanford, all of whom helped us track down, collect, and interpret the leveling data. Part of this work was supported by the Centre National de Recherche Scientifique (G.E.) and the Institut de Physique du Globe de Paris (G.E. and R.S.S.). G.E. was further supported by the U. S. Geological Survey and by the National Science Foundation grants EAR89-16250 and EAR91-05733.

REFERENCES

Allen, R. V., Automatic phase pickers: Their present use and future prospects, *Bull. Seismol. Soc. Am.*, *72*, S225–S242, 1982.

Barrientos, S. E., R. S. Stein, and S. N. Ward, Comparison of the 1959 Hebgen Lake, Montana and the 1983 Borah Peak, Idaho, earthquakes from geodetic observations, *Bull. Seismol. Soc. Am.*, *77*, 784–808, 1987.

Brune, J. N., Tectonic stress and spectra of seismic shear waves from earthquakes, *J. Geophys. Res.*, *75*, 4997–5009, 1970. (Correction, *J. Geophys. Res.*, *76*, 5002, 1971.)

Bull, W.B., Land subsidence due to ground-water withdrawal in the Los Banos-Kettleman City area, California, 2, Subsidence and compaction of deposits, *U.S. Geol. Surv. Prof. Pap., 437-F*, 89 pp., 1975.

Conservation Committee of California Oil Producers, Annual review of California oil and gas production, Los Angeles, 1974–1987.

Das, S., and K. Aki, Fault plane with barriers: A versatile earthquake model, *J. Geophys. Res.*, *82*, 5658–5670, 1977.

Dziewonski, A. M., and J. H. Woodhouse, An experiment in systematic study of global seismicity: Centroid-moment tensor solutions for 201 moderate and large earthquakes of 1981, *J. Geophys. Res.*, *88*, 3247–3271, 1983.

Dziewonski, A. M., T. Chou, and J. H. Woodhouse, Determination of earthquake source parameters from waveform data for studies of global and regional seismicity, *J. Geophys. Res.*, *86*, 2825–2852, 1981.

Eaton, J. P., The earthquake and its aftershocks from May 2 through September 30, 1983, in The Coalinga, California Earthquake of May 2, 1983, edited by M. Rymer and W. Ellsworth, *U.S. Geol. Surv. Prof. Pap., 1487*, 113–170, 1990.

Eaton, J. P., M. E. O'Neill, and J. N. Murdoch, Aftershocks of the 1966 Parkfield-Cholame, California, earthquake: A detailed study, *Bull. Seismol. Soc. Am.*, *60*, 1151–1197, 1970.

Eberhart-Phillips, D., Active faulting and deformation of the Coalinga anticline from three-dimensional velocity structure and seismicity, *J. Geophys. Res.*, *94*, 15,565–15,586, 1989*a*.

Eberhart-Phillips, D., Investigations of crustal structure and active tectonic processes in the Coast ranges, central California, Ph.D. thesis, Stanford Univ., Stanford, Calif., 1989*b*.

Eberhart-Phillips, D., Three-dimensional P and S velocity structure in the Coalinga region, California, *J. Geophys. Res.*, *95*, 15,343–15,364, 1990.

Ekström, G., A very broad band teleseismic analysis of the August 4, 1985, North Kettleman Hills earthquake, *EOS Trans. AGU*, *67*, 1223, 1986.

Ekström, G., A broad band method of earthquake analysis, Ph.D. thesis, Harvard Univ., Cambridge, Mass., 1987.

Ekström, G., A very broad band inversion method for the recovery of earthquake source parameters, *Tectonophysics*, *166*, 73–100, 1989

Ekström, G., and A. M. Dziewonski, Centroid-moment tensor solutions for 35 earthquakes in western North America (1977–1983), *Bull. Seismol. Soc. Am.*, *75*, 23-39, 1985.

Ekström, G., and E. R. Engdahl, Earthquake source parameters and stress distribution in the Adak Island region of the central Aleutian Islands, *J. Geophys. Res.*, *94*, 15,499–15,519, 1989.

Hanks, T., and H. Kanamori, A moment magnitude scale, *J. Geophys. Res.*, *84*, 2348–2350, 1979.

Hartzell, S. H., and T. H. Heaton, Teleseismic mechanism of the May 2, 1983 Coalinga, California, earthquake from long-period P-waves, in The 1983 Coalinga, California Earthquake, *Spec. Publ. Calif. Div. Mines Geol.*, *66*, 241–246, 1983.

Harvey, D., and G. L. Choy, Broadband deconvolution of GDSN data, *Geophys. J. R. Astron. Soc.*, *69*, 659–668, 1982.

Hauksson, E., and L. M. Jones, The 1987 Whittier Narrows earthquake sequence in Los Angeles, southern California: Seismological and tectonic analysis, *J. Geophys. Res.*, *94*, 9569–9589, 1989.

Hill, D. P., J. P. Eaton, and L. M. Jones, Seismicity 1980–1986, in The San Andreas Fault System, California, edited by R. E. Wallace, *U.S. Geol. Surv. Prof. Pap., 1515*, 115–152, 1990.

Hill, M. L., Earthquakes and folding, Coalinga, California, *Geology*, *12*, 711-712, 1984.

Holdahl, S. R., W. E. Strange, and R. J. Harris, Empirical calibration of Zeiss Ni1 level instruments to account for magnetic errors, *Tech. Memo. NOS NGS-45*, 23 pp., Natl. Geod. Surv., Rockville, Md., 1986.

Kanamori, H., and D. L. Anderson, Theoretical basis for some empirical relations in seismology, *Bull. Seismol. Soc. Am.*, *65*, 1073–1095, 1975.

Kawasumi, H., *General Report on the Niigata earthquake of 1964*, 550 pp., Tokyo Electrical Engineering College Press, Tokyo, 1973.

King, G. C. P., and M. Ellis, The origin of large local uplift in extensional regions, *Nature*, *348*, 689–693, 1990.

Lin, J., and R. S. Stein, Coseismic folding, earthquake recurrence, and the 1987 source mechanism at Whittier Narrows, Los Angeles basin, California, *J. Geophys. Res.*, *94*, 9614–9632, 1989.

McGarr, A., On a possible connection between three major earthquakes in California and oil production, *Bull. Seismol. Soc. Am.*, *81*, 948–970, 1991.

Meltzer, A., Crustal structure and tectonic evolution: Central California, Ph.D. thesis, Rice Univ., Houston, Tex., 1989.

Namson, J.S., and T.L. Davis, Seismically active fold and thrust belt in the San Joaquin Valley, central California, *Geol. Soc. Am. Bull.*, *100*, 257–273, 1988.

Obradovich, J.D., C.W. Naeser, and G.A. Izett, Geochronology of late Neogene marine strata in California, Correlation of tropical through high-latitude marine Neogene deposits of the Pacific basin, *Stanford Univ. Publ. Geol. Sci., XIV*, 40-41, 1978.

Packard, R. F., and J. H. MacNeil, A direct comparison of spirit and compensator leveling, *Geophys. Res. Lett.*, *10*, 849–851, 1983.

Reasenberg, P., and D. Oppenheimer, FPFIT, FPPLOT and FPPAGE: FORTRAN computer programs for calculating and displaying earthquake fault-plane solutions, *U.S. Geol. Surv. Open File Rep., 85-739*, 1985.

Reches, Z., and M. D. Zoback, Theoretical analysis of the deformation of a layered sequence above a fault – Preliminary application to the Loma Prieta earthquake, Chapter X, in *Stanford Rock Physics and Borehole Geophysics*, vol. 40, Stanford University, Stanford, Calif., 1990.

Rockwell, T., Neotectonics of the San Cayetano fault, Transverse Ranges, California, *Geol. Soc. Am. Bull.*, *100*, 500–513, 1988.

Rodgers, D. A., and W. D. Rizer, Deformation and secondary faulting near the leading edges of a thrust fault, in *Thrust and Nappe Tectonics*, edited by K. R. McClay and N. J. Price, pp. 65–77, Geological Society of London, Oxford, England, 1981.

Roeloffs, E. A., S. S. Burford, F. S. Riley, and A. W. Records, Hydrologic effects on water level changes associated with episodic fault creep near Parkfield, California, *J. Geophys. Res.*, *94*, 12,387–12,402, 1989.

Rumpf, W. E., and H. Meurisch, Systematische Änderungen der Ziellinie eines Präzisions Kompensator-Nivilliers – inbesondere des Zeiss Ni1 – durch magnetische Gleich- und Wechselfelder, paper presented at XVI FIG Congress, Montreux, Switzerland, 1981.

Sarna-Wojiciki, A. M., K. R. Lajoie, C. E. Meyer, D. P. Adam, and H. J. Rieck, Tephrochronologic correlation of upper Neogene sediments along the Pacific margin, conterminous United States, in *The Geology of North America*, vol. K-2, *Quaternary of the Non-Glacial U.S.*, edited by R. Morrison, pp. 117–140, Geological Society of America, Boulder, Colo., 1991.

Segall, P., Stress and subsidence resulting from subsurface fluid withdrawal in the epicentral region of the 1983 Coalinga earthquake, *J. Geophys. Res.*, *90*, 6801–6816, 1985.

Stein, R. S., and G. Ekström, Seismicity and geometry of a 110-km-long blind thrust fault, 2, Synthesis of the 1982–1985 earthquake sequence, *J. Geophys. Res.*, this issue.

Stein, R. S., and G. C. P. King, Seismic potential revealed by surface folding: 1983 Coalinga, California, earthquake, *Science*, *224*, 869–872, 1984.

Stein, R. S., and R. S. Yeats, Hidden earthquakes, *Sci. Am.*, *260*, 48–57, 1989.

Stover, C. W., Intensity distribution and isoseismal map, in The 1983 Coalinga, California Earthquake, *Spec. Publ. Calif. Div. Mines Geol. 66*, 1–4, 1983.

Stover, C. W., and L. R. Brewer, United States earthquakes, 1985, *U.S. Geol. Surv. Bull. 1954*, 170 pp., 1991.

Strange, W. E., Empirical determination of magnetic corrections for Ni1 level instruments, in *Proceedings of 3rd International Symposium on North American Vertical Datum*, edited by D. B. Zilkoski, pp. 363–374, National Geodetic Information Center, NOAA, Rockville, Md., 1985.

Thurber, C. H., Earthquake locations and three-dimensional crustal structure in the Coyote Lake area, central California, *J. Geophys. Res.*, *88*, 8226–8236, 1983.

Wentworth, C. M., and M. D. Zoback, The style of late Cenozoic deformation at the eastern front of the California Coast ranges, *Tectonics*, *8*, 237–246, 1989.

Wentworth, C. M., and M. D. Zoback, Structure of the Coalinga area and thrust origin of the earthquake, in The Coalinga, California Earthquake of May 2, 1983, edited by M. Rymer and W. Ellsworth, *U.S. Geol. Surv. Prof. Pap., 1487*, 41–68, 1990.

Wetmiller, R. J., R. B. Horner, H. S. Hasegawa, R. G. North, M. Lamontagne, D. H. Weichert, and S. G. Evans, An analysis of the 1985 Nahanni earthquakes, *Bull. Seismol. Soc. Am.*, *78*, 590–616, 1988.

Woodring, W. P., R. B. Stewart, and R. W. Richards, Geology of the Kettleman Hills oilfield, *U.S. Geol. Surv. Prof. Pap., 195*, 170 pp., 1940.

Yeats, R. S., Active faults related to folding, in *Active Tectonics*, pp. 63–79, National Academy Press, Washington, D. C., 1986.

Zigler, J. L., C. M. Wentworth, and J. A. Bartow, Structure contour map of the tops of the Kreyenhagen formation and Cretaceous strata in the Coalinga area, Fresno and Kings counties, California, *U.S. Geol. Surv. Misc. Field Stud. Map, MF-1843*, 1986.

J. P. Eaton, D. Eberhart-Phillips, and R. S. Stein, U.S. Geological Survey, 345 Middlefield Road, MS 977, Menlo Park, CA 94025.

G. Ekström, Department of Earth and Planetary Sciences, Harvard University, 20 Oxford Street, Cambridge, MA 02138.

(Received April 16, 1990;
revised January 18, 1991;
accepted April 10, 1991.)